Nanoscale

Accepted Manuscript

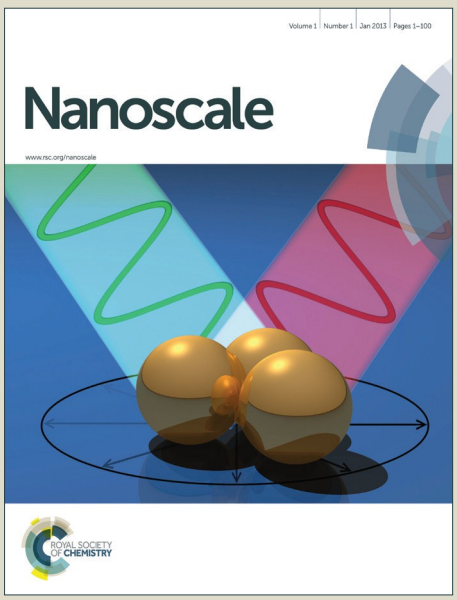

ROYAL SOCIETY OF CHEMISTRY

www.rsc.org/nanoscale

Faceted Metal and Metal Oxide Nanoparticles: Design, Fabrication and Catalysis

Jaya Pal and Tarasankar Pal*

Department of Chemistry, Indian Institute of Technology, Kharagpur-721302, India

E-mail: tpal@chem.iitkgp.ernet.in

Abstract:

The review addresses new advancement of metal, bimetallic, metal oxide, and composite particles in their nanoregime for facet selective catalytic application. Synthesis and growth mechanism of the particles have been accounted in brief in this review with a view to elaborate critical examination of the faceted morphology of the particles for catalysis. Now size, shape and composition of the particles have been found to become largely overruled and remain subdued because precise explanation now emerges out from the facet selective catalysis. Thus selective high and low index facets have been found to regulate the selective promotion of adsorption which eventually leads to effective catalytic reaction. As a consequence high density of atoms on a catalyst surface rest at the corners, steps, stages, kinks etc. to host the adsorbate efficiently which catalyze a reaction. Again, surface atomic arrangement and bond length has been found to play dominant role for adsorption leading to effective catalysis.

1. Introduction

The past decade has witnessed the size,[1-6] shape,[7-15] and composition[16-22] dependent catalytic reactivity of nanoparticles. By tuning the size, shape and composition, the catalytic activity of a nanomaterial can be improved. It is well established that a catalyst becomes more effective as its size goes down. More precisely this fact can be envisaged from the increased number of

surface atoms especially from the general idea of surface to volume ratio. Thus size dependent catalysis becomes an important aspect in the surface catalysed reaction. It has already been proved that reduction potential of metal particles becomes progressively negative as the size goes down (Fig. 1).[23,24]

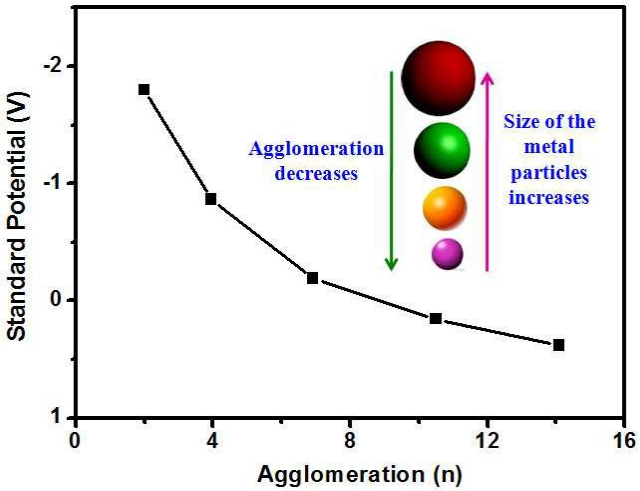

Fig.1. Electrochemical standard potential of metal particles depends on agglomeration number.

Again, the catalytic reactivity of nanoparticle is also related with the shape of particles. The shapes of the nanocatalysts are determined by their crystal structures, including crystallinity, terminating facets and anisotropy. These parameters strongly affect the properties of nanocatalysts. For example, shape dependent catalysis by Au nanoparticles was reported by Liang and co-workers who have used Au nanoparticles in the form of nanospheres, nanorods, and nanoprisms to catalyze the hydrogenation of aromatic nitro-compounds to amines.[25] Furthermore, multi-component nanocomposites with controlled composition can greatly alter the catalytic reactivity as well. This issue is interesting because in one hand, it can advance

the fundamental understanding of solid state reactivity; on the other hand, it might provide a facile method to tune the composition for enhanced catalytic effect. Recently the exposed facet of a nanocrystal has been found to offer greater versatility than size, shape and other parameters in tuning the catalytic efficiency of nanocrystal.[26-28] Facets are the flat faces on particular geometric shapes. Generally the shape of a nanoparticle has a strong correlation with the exposed facet(s) and thus the surface structures as well as the fraction of atoms at corners and edges also become important.[29,30] Faceted nanomaterials are of two types: (i) low-index faceted nanomaterials and (ii) high-index faceted nanomaterials. Since a facet, a surface of a crystal, is a plane, it can also be denoted with miller indices. Low index facet is one where the sum of the three components is small. High index facets are those which contain a set of Miller indices {hkl} with at least one index greater than unity.

During the synthesis of faceted metal or metal oxide nanoparticles, if the growth is under thermodynamic control, the product will be bounded by low-index facets i.e., lower surface energy. In this case, the stabilizing or capping agent plays an imperative role for determining the products shape because the different facets have selective adsorption properties which is also reflected in their growth rates.[31] In contrast, when the growth is governed under kinetically controlled condition, then the product can drastically diverge from the thermodynamically favoured structure; noteworthy examples include nanocrystals with high-index facets or concave surfaces.[32] The difficulty in generating concave structures with controlled high-index facet can be attributed to their higher surface energy.[33,34] In this case, the use of a capping agent, a template, and/or kinetic control has been considered for nanocrystals formation with concave surfaces. Metal and metal oxide nanostructures with high index facets possess more active catalytic sites than usual due to the presence of high density of low-coordinated atoms, steps, edges and kinks and now it becomes an important arena in catalysis.[35] So for enhanced catalytic activity, design and fabrication high index

faceted metal or metal oxide nanoparticle is now a challenging task. Recent studies revealed that high index faceted nanocrystals are synthesized either by selective overgrowth or through site-specific dissolution of nanoparticles.

The most widely studied facet-dependent property is catalytic reactivity of nanomaterials towards a particular reaction because the catalytic activity of nanomaterials is highly related to their exposed facets. This is understandable because the atoms at different facets have different reactivity/surface energy. Another interesting facet dependent property is revealed out of the facet selective etching and reshaping of polyhedral nanocrystals, showing that surface conditions such as charges and preferential molecular adsorption on selected faces can be exploited even to form unique hollow or concave structures.[36-39] There are also reports addressing facet dependent electrical conductivity[40] and magnetic behaviour[41] of different nanoparticles. Currently, facet dependent synthesis of different nanoparticles is making the headlines in the research area due to their promising properties and enhanced catalytic reactivity.

A wide variety of methods has been developed for synthesis of noble metals, including Au,[42-45] Ag,[46-49] Pd,[50-53] Pt,[54-57] and Rh[58-61] as well as their bimetallic[62-65] combinations with different exposed facets. For noble metals, the most commonly observed shapes are octahedron, truncated octahedron, cuboctahedron, and cubes, with different degrees of truncation at corners and edges and enclosed by different low-index facets, such as {111}, {110}, {100} in different proportions (Fig. 2). Such types of materials with faceted structures have received immense importance due to their outstanding performance in catalytic reaction such as Suzuki coupling,[66-68] CO oxidation,[69-72] styrene oxidation,[48] hydrogenation,[73-78] and electrocatalytic reaction[79-85].

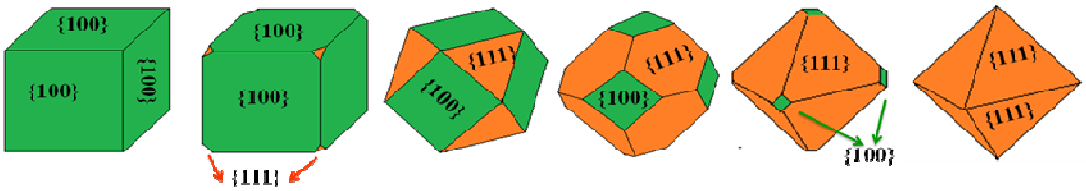

Fig. 2. 3-D Geometry of different polyhedrons with different volume ratio of {100} to {111} facets.

It is well known that the Pt-groups of metals are very costly due to their extremely low abundance in the Earth's crust. But due to the enhanced catalytic activity, higher stability of the particle and minimum poisoning effect from the external agencies, there is a continuous and ever-increasing demand and hence surge for synthesis of such type faceted noble nanomaterials. In order to reduce the use of these expensive metals, we need to focus on the performance of more familiar, low cost and stable oxide materials such as Cu_2O,[86,87] TiO_2,[88-90] ZnO,[91,92] Fe_2O_3,[93] Co_3O_4[94,95]etc. Thus the recent trend of the research area has been shifted towards the design and fabrication of such type low cost oxide nanomaterials by controlling their shapes with exposing different reactive facets. To this end, a variety of different shaped oxide nanomaterials have been reported for their enhanced catalytic reactivity in different fields such as photocatalysis,[96,97] gas sensor,[98] lithium-ion battery,[99] solar energy conversion,[100,101] and water splitting[102].

In this review, we focus on the facet dependent catalytic activity of metal, metal oxide, and composite nanomaterials with low and high index facets. For each material, we briefly summarise the progress towards the experimental implementation of these synthetic approaches. We also investigated the essential role of stabilizing or capping agent in determining the products shape with exposed facet by tuning the surface reactivity of

different facets via selective adsorption. Finally, the dramatic differences in catalytic reactivity with distinctly different facets are addressed in terms of surface energy, surface atomic arrangement and configuration associated with terraces, steps, kinks, and vacancies. As many reviews on Pt-group of metals,[103,104] Cu_2O[38] and celebrated TiO_2[105,106] have already been reported hence in this brief report we mostly centred our discussion for the faceted other common and useful oxide nanomaterials.

2. Low Index Faceted Nanomaterials

Metal and metal oxide nanoparticles expose different low-index facets depending on the particle shapes. Octahedral, cubic and rhombic dodecahedral nanocrystals are bound by {111}, {100} and {110} low-index facets, respectively. Facet-dependent catalytic activity can be appraised more accurately if only a single set of surface facets are available in the nanocrystals. The catalytic reactivity of the particles exposing two or more surface facets such as truncated octahedra and cuboctahedra can also be examined, when their efficiencies are compared to the monofaceted nanocrystals.

2. 1. Metal Nanoparticles

During the last few decades, the synthesis of metal nanoparticles with variable shapes by exposing specific crystal facets has received noteworthy interest due to their potential and promising application in facet selective catalysis. A careful review of literature reveals that the platinum metals by virtue of their nobility and partially filled d-orbital become the most celebrated catalyst. It is also observed that especially Pd remains to be the best for hydrogenation reaction. In this context if we consider the morphology driven or facet selective catalysis even then Pt and Pd takes the lion's share. Even today electrocatalysis is best prompted by faceted Pt and Pd nanoparticles.

2.1.1. Platinum Nanoparticles

El-Sayed and coworkers investigated the facet dependent catalytic reactivity of Pt nanoparticles with varied shapes for electron-transfer reaction between hexacyanoferrate and thiosulfate.[107-111] For example the tetrahedron Pt nanoparticle containing {111} facets exhibited highest catalytic activity than {100} faceted Pt nanocube.[107] Furthermore comparative study of hydrogenation reaction with facet-controlled Pt nanoparticles was conducted in great detail by Somorjai *et al*.[122-116,77,78] They examined that {100} faceted Pt nanocubes produced cyclohexane as the major products during hydrogenation of benzene whereas cuboctahedron bound by {111} and {100} facets produced a mixture of cyclohexane and cyclohexene.[112] Faceted Pt nanoparticles are also widely used in electrocatalytic oxygen reduction reaction (ORR). In 1994, Yeager *et al*. proved that catalytic reactivity towards ORR decreased in the sequence of {110} > {111} > {100}.[117] ORR was found to be sensitive to the exposed crystal facets of the Pt electrode surface. Xia *et al*. investigated that Pt mutioctahedron served as a better catalyst for ORR than the commercial Pt/C due to the high ratio of {111} to {100} as exposed facets and the existence of surface steps on their surfaces.[118] In another work Sun *et al*. proved {100} faceted Pt nanocube exhibited four times higher specific activity for ORR than from other faceted polyhedrons or truncated cubes.[119.120]

As the shape control synthesis of nanoparticles is believed to be a kinetic process, high energy facet vanishes faster in crystal growth stage and difficult to preserve on surface of the nanoparticles. Therefore capping agents (surfactants or biomolecules or peptides) are used to overcome this problem in the shape control synthesis of nanoparticles. Capping agent can bind specifically to the particular facet with lowering the surface energy. In this study shape controlled Pt nanocrystals have been obtained by using appropriate peptide sequence.[121] The {100} faceted Pt cubes have been synthesized by binding peptide Ac–Thr–Leu–Thr–Thr–

Leu–Thr–Asn–$CONH_2$ and {111} facet Pt tetrahedrons have been synthesized by binding peptide Ac–Ser–Ser–Phe–Pro–Gln–Pro–Asn–$CONH_2$. Again the shape transformation from cube to tetrahedron is done at room temperature by switching the binding peptide sequence.

Huang *et al*. reported the preparation of Pt nanocrystals in presence of different aromatic molecules.[122] There facet selective capping by differently substituted organic molecules evolves differently faceted Pt nanocrystals. The confirmation obtained from Raman study. Again the study has been generalized considering facet selective synthesis of Pd nanocrystals also. In one case they have provided aromatic organic molecules which bear negative ring current i.e., negative electrostatic potential because of the substitution in the phenyl ring. In that case phenyl ring is able to interact with the {111} facets of Pt nanocrystals. However, electron withdrawing substituents in the phenyl ring makes the ring current positive. As a result of which molecules like p-nitro phenol does not interact with the {111} facet instead {100} facet extend its partnership with the positively charge bearing p-nitro phenol like molecules.

Keeping this idea in mind, it might be possible to think of a junction between two differently faceted nanomaterials for catalysis. There two selective capping agents may be brought into contact because of their facet selective capping by the two faceted nanomaterials in contact. Thus a facile reaction between two capping agents might take place across the hetero-junction.

2.1.2. Palladium Nanoparticles

Pd nanoparticles enclosed by different facets are also widely used in hydrogenation,[123-127] Suzuki coupling,[128-132] oxygen reduction[133] and formic acid oxidation reaction[134]. For selective hydrogenation reaction of 1,3-butadiene, it was found that {110} faceted Pd single crystals exhibited five times higher catalytic reactivity than {111} facet exposed Pd[135,136]

indicating more open surface and higher sticking probability of {110} facets which favours adsorption and activation.[137] The product selectivity also varies with different exposed facets. For example, {111} faceted Pd nanoparticle produced fully hydrogenated product of n-butane whereas both 2-butene and n-butane were obtained on the {110} surface.[138-140]

Although Pt is the most efficient catalyst for ORR but the researchers has been devoted for alternative catalyst due to its high cost and Pd (less expensive than Pt) is probably the best substitute among all other metals around Pt. Xia *et al*. recently studied facet dependent ORR activity of {100} faceted Pd cubes and {111} faceted Pd octahedron.[133] Facet dependent formic acid oxidation had also been explained by taking five differently shaped Pd based catalysts. It was found that maximum current density increased in the order of octahedrons < truncated octahedrons < cuboctahedrons < truncated cubes < cubes (Fig. 3) signifying that {100} facet was more reactive for the oxidation of formic acid than that of {111} facet.[134]

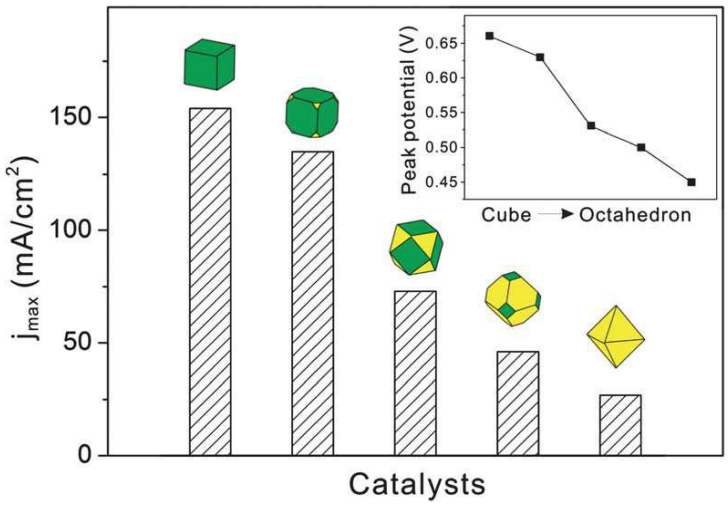

Fig. 3. Maximum current densities of formic acid oxidation obtained by using different Pd polyhedrons enclosed by {111} and {100} planes in different proportions. The inset displays their corresponding peak potentials. Reprinted with permission from ref. 134. Copyright 2012 from Royal Society of Chemistry.

In another approach, Xia *et al*. prepared size dependent Pd octahedrons from Pd cubes of a single size.[141] There selective capping agent Br^- hindered the oxidative etching of Pd on {100} facet as a result of which selectively {111} facets have been found to be etched. Presence of a suitable reducing agent triethylene glycol in solution phase reverts back the oxidized Pd(II) to Pd(0). The freshly produced Pd(0) gets deposited back on the edges of the cube and diffuse to the adjacent side faces because of the ongoing oxidation and Br^- ion blocked {100} facets (Fig. 4). Thus octahedral Pd nanocrystals are produced. Size dependent octahedrons have been produced just by controlling the etching and regrowth rate of Pd by variable proportion of oxidant and reductant.

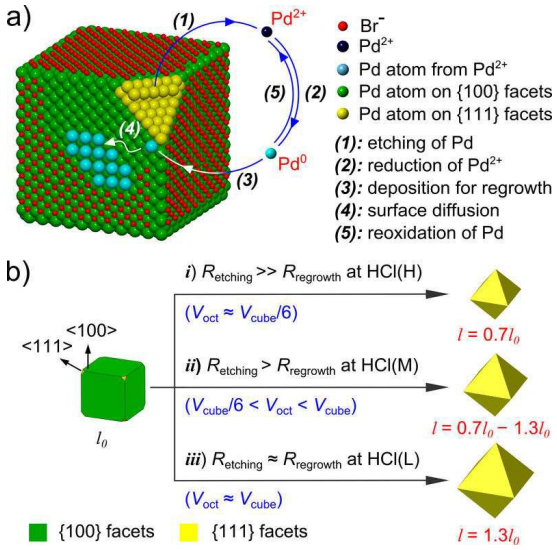

Fig. 4. (a) Schematic representation of the five important steps involved in the oxidative etching and regrowth process. (b) Schematic representation of the formation of Pd octahedra with different but controllable edge lengths (l) by controlling the rates of oxidative etching and regrowth for Pd cubes. Reprinted with permission from ref. 141. Copyright 2013 from American Chemical Society.

The presence of bromide ions in the reaction mixture plays a vital role for formation of {100} faceted Pd and Ag nanocrystals.[142-145] Here bromide ions act as a capping agent and preferentially adsorb on the {100} facets, thus stabilizing these facets. In this work, Xia *et al*. measured the number of Br^- ions adsorbed on the surface of a {100} faceted Pd nanocubes using inductively coupled plasma mass spectrometry and X-ray photoelectron spectroscopy.[146] Again from XPS analysis it is also confirmed that there is a chemisorptions type of interaction between Br^- ions and Pd nanocubes which can be removed only by deposition at higher temperature under reductive condition. The removal of adsorbed Br^- ions on the surface of {100} faceted Pd nanocubes is also possible through over growth of Pd cube which causes the formation of cuboctahedral or octahedral structures. A critical amount of Br^- ions is required for full coverage of all the {100} facets and if the amount is less than the optimum value then it causes the formation of truncated cubes with some {111} facets. Thus I^- and Br^- deserve special mention in relation to oxidative etching as well as capping of Pd crystal facets.

2.1.3. Gold Nanoparticles

Coinage metal Au as nanoparticle has attracted extensive interest in heterogeneous catalysis. But their facet dependent phenomenon is far less explored even though it appears as a hot topic in the catalysis research. Zubarev *et al*. demonstrated the wet chemical process for the purification of high aspect ratio 1-D Au nanorods from the initial mixture of Au nanoparticles (rods and platelets).[147,148] Here Au nanoparticles have been synthesized by using the concept of seed mediated technique, first proposed from our laboratory in 2001,[6] where a mixture of spheres, rods and platelets are obtained. It is observed that the treatment of the mixture of rods and platelets with Au(III)/ CTAB complex causes a conversion of platelets into higher soluble smaller nanodisks, which remain in the supernatant while the pure nanorods slowly precipitate (Fig. 5). Supernatant blue solution containing nanodisks can be easily converted

back to less soluble multifaceted platelets only by addition of Au(I) ions and ascorbic acid. It has been accomplished that in general Au fcc planes follows the energy sequence {111} < {100} < {110}. However, experimentally a different order has often been observed in the solution phase {111} < {110} < {100}. So adsorption of capping agent significantly altered the surface energy of the faceted particles.

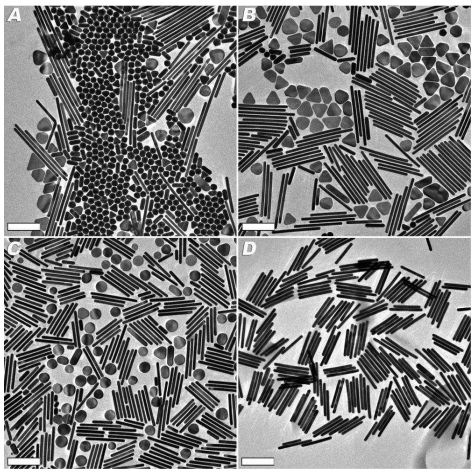

Fig. 5. TEM images of gold nanoparticles: (A) as-synthesized mixture, (B) mixture of faceted platelets and rods, (C) mixture of nanodisks and rods and (D) nanorods. Reprinted with permission from ref. 147. Copyright 2008 from American Chemical Society.

In a recent work, nitro aromatic reduction has been studied by using different faceted Au nanoparticles (cubic, octahedral, and rhombic dodecahedral) at different temperatures.[149] Highest catalytic rate of reduction has been observed for rhombic dodecahedron irrespective of the temperature change. From DFT calculations, it has been found that the binding energy between p-nitroaniline and {110} facets of rhombic dodecahedral Au nanoparticles is higher than the other two and the catalytic efficiency follows the sequence of {110} > {100} > {111}. It was also observed that at 25˚C {100} faceted cubic Au nanoparticles exhibited higher reduction rate than from {111} faceted Au and the situation is just reversed at 40˚C.

Recently, regioselective catalysis using morphologically different Au nanocrystals for the synthesis of 1,4-disubstituted triazole through click reaction has been reported by Huang *et al*.[150] It is observed that rhombic dodecahedral Au nanocrystal with {110} facet serves as a best suited catalyst for the regioselective synthesis of 1,4-disubstituted triazole than from {111} faceted octahedral and {100} faceted cubic Cu_2O nanocrystals. The improved catalytic efficiency of rhombic dodecahedral Au nanocrystal can be attributed to the less-congested surface Au-atom arrangement on the {110} surface and largest unsaturated coordination number of surface Au atoms.

So, there is a need of further experimentation to explore the facet selective catalysis especially for Au nanocrystals.

2.1.4. Rhodium Nanoparticles

Facet dependent catalytic reactivity of differently shaped Rh nanoparticles is less explored with respect to Pt, and Pd. Rhodium 1D nanostructure has been prepared from aqueous $RhCl_3$ solution from uniform heating in presence of CTAB. Here CTAB acts as a face selective adsorption additive and helped the formation of 1D nanostructures of Rh.[151] It has been observed that the pH has a remarkable influence on the alteration of aspect ratio and sharpening of the edges of Rh nanorods. Interesting shape transformation has also been shown in a selective redox environment for nanorods and nanowires to octahedral and spherical particles, respectively.

Attention has been directed to evolve concave nanocrystals of Rh encasing mix {111} and {110} facets as Rh is an important catalyst.[152] Selective capping of {111} facet of Rh seed particle by citrate and then temperature dependent diffusion of Rh from corner to edge gives birth to concave tetrahedron (Fig. 6). This synthetic strategy offers a radically different approach for formation of noble-metal nanocrystals with concave surfaces.

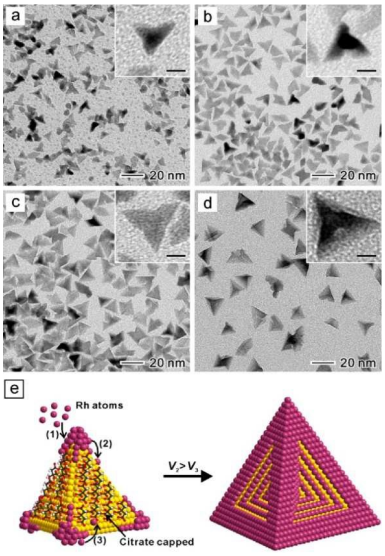

Fig. 6. (a−d) TEM images of Rh nanoparticles obtained at different reaction times after the injection of Rh(III) precursor: (a) 6, (b) 15, (c) 30, and (d) 60 min, respectively. All the scale bars are 5 nm. (e) Schematic representation of the formation of Rh concave tetrahedrons. Reprinted with permission from ref. 152. Copyright 2013 from American Chemical Society.

2. 2. Bimetallic Nanoparticles

Catalytic reactions involving mono metallic particles have served many industrial processes. Latter on it has been experienced that bimetallic or even multimetallic particles are more advantageous in catalytic performance and optical properties than single component system.[153-158] In this respect noble metal bimetallic particles are very important. Recently Pt-Pd, Pd-Rh, Pd-Ag, Pd-Ir, Pt-Au and Co-Pt_3 etc. have been used for catalytic purposes.

Bimetallic alloy nanoparticles of Pt-Pd bearing nanotetrahedron (Td) and nanocubes (Cb) have been meticulously synthesized via one-pot hydrothermal route.[159] Reducing agent, HCHO together with capping agent, $Na_2C_2O_4$ evolve nanotetrahedron (Td) from the solution phase synthetic route. The capping agent as well as the oxidized product of HCHO co-jointly

help the selective evolution of Td. However, nanocubes (Cb) are obtained while PVP is used as reducing agent and iodide-bromide as small capping agents. Interchange of reducing agent resulted in mixture of morphologically different products. It has been shown that {100} facet bound cube has higher electrocatalytic activity than {111} faceted Td towards methanol oxidation. Interestingly, {111}-facet enclosed Pt-Pd Td exhibits better durability.

For the fuel cell application i.e., from the electro-oxidation point of view Co/Pt_3 has recently been exploited for methanol oxidation.[160] Zhang and co-workers have synthesized morphologically different shapes of Co/Pt_3 using variable proportion of stabilizing agents. The {111} faceted nanoflowers exhibited highest catalytic efficiency towards methanol oxidation than any other facets even though there happens size variation of the nanocrystals of Co/Pt_3.

In another piece of work chosen single capping agent PAH (poly allyl amine hydrochloride) has been found as a complex forming and tuning agent to co-reduce of Pt and Au precursor salts to form high energy {100} faceted Pt/Au alloy nanocube for 4-Nitrophenol reduction.[161]

Xia and co-workers reported the preparation of three distinctive shapes of Pd-Ag bimetallic nanocrystals through controlled nucleation and growth of Ag atom on one, three, and six of the equivalent {100} facets of a Pd seed.[162] Only by controlling the flow rate of $AgNO_3$, they obtained hybrid dimers, eccentric nanobars, and core–shell type of Pd-Ag nanocrystals. These Pd-Ag bimetallic nanoparticles exhibited significantly different localized surface plasmon resonance properties in comparison to pure metals and their alloys.

Considering the importance of bimetallic catalyst particles recently Xia *et al*. have considered Rh deposition on selected facets of Pd nanocrystals.[163] Three important parameters have been introduced for fabrication of bimetallic Pd-Rh particles using the concept of seed mediated technique. Monometallic basic frame work of cuboctahedron Pd nanocrystals has become the

selected platform for deposition of Rh metal. Two important ideas have enriched the {111} facet of Pd cuboctahedron by Rh due to (i) selected capping of {100} facet of Pd by Br^- ion and (ii) thermodynamically controlled reduction of Rh(III) ions onto the selected part of {111} facet of Pd. In the latter case slow but controlled reduction covers the entire {111} facet of Pd producing Pd-Rh cubic structures (Fig. 7). Whereas faster rate of reduction produce multiple Rh island on each Pd {111} facets due to high surface energy and inter atomic Rh-Rh binding energy (Fig. 7). Finally etching of Pd-Rh bimetallic nanocrystals by Fe(III)/Br^- pair produced Rh nanoframe.

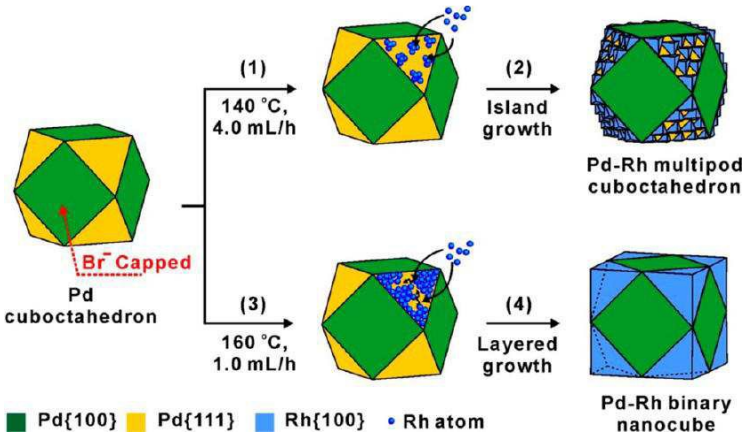

Fig. 7. Schematic illustrations of the formation of Pd−Rh multipod cuboctahedron and Pd−Rh binary nanocube from Pd cuboctahedron. Reprinted with permission from ref. 163. Copyright 2013 from American Chemical Society.

Recently the synthesis of hollow structure or concave faces has received noteworthy attention due to presence of high-index facets as well as their unique optical and catalytic properties.[164-172] Xia *et al.* have reported the synthesis of Pd-Rh core-frame concave nanocubes through site-specific over growth of Rh adatoms at the corners and edges of Pd cubic seeds.[173] The as-synthesized Pd cubic seeds are slightly truncated at the corners and

edges. It is observed that Br- ions cover the Pd {100} surface except the truncated sides of the Pd cube. So Rh atoms deposited at all the corners and edges and ultimately formed Pd-Rh concave core-frame structure with Pd {100} and Rh {110} facets (Fig. 8). Rh is highly resistant to oxidative corrosion than from Pd.[174,175] So etching of Pd-Rh core-frame concave nanocubes by Fe(III)/Br^- pair produced Rh nanoframes with a unique open structure through selective etching of the Pd cores (Fig. 8).

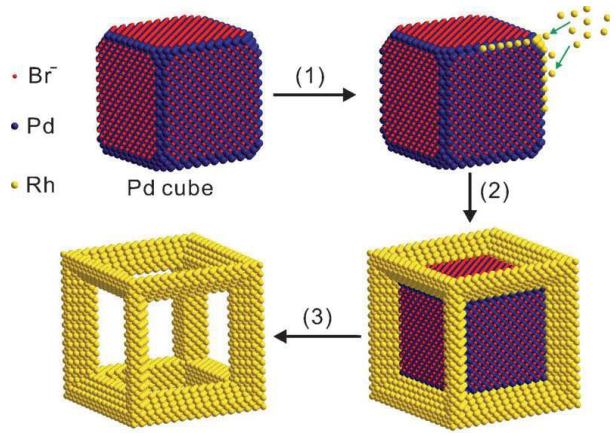

Fig. 8. Schematic representation of the synthesis of Pd-Rh core–frame concave nanocubes and Rh cubic nanoframes by using three important steps: (1) Selective nucleation of Rh at the corners and edges of the Pd nanocubes due to the capping of {100} facets by Br^- ions; (2) formation of concave nanocubic Pd-Rh bimetallic core–frame since the growth of Rh on the corners and edges of the Pd nanocubes is continued; and (3) preparation of Rh cubic nanoframes by selectively etching away the Pd cores. Reprinted with permission from ref. 173. Copyright 2012 from Wiley-VCH Verlag GmbH & Co.

As Pt-group metals are very expensive, researcher focused on synthesis of shape and size dependent synthesis of nanocrystals with maximise their catalytic performance.[176] Iridium nanoparticles generally exist with morphology of spherical shapes in which investigation of facet dependent catalytic activity is impossible.[177-180] So synthesis of Iridium nanocrystals with well-defined facets is now a challenging task. Keeping this in mind, Xia *et al*. for the first time reported the facile synthesis of Ir nanocrystals with well-defined facets through a simple seed-mediated growth approach where cubic and octahedral Pd nanoparticles are used as seeds.[181] The main success of the reaction is that layer-by layers smooth deposition of Ir shell on Pd core due to fast diffusion of Ir adatoms on Pd surface which is greatly accelerated at high temperature (200˚C). It is found that cubic and octahedral Pd@Ir core-shell nanostructures are also enclosed by {100} and {111} facets as like the initial Pd seeds which ensure the replication of facets. Then these two well-faceted core-shell nanocrystal exhibited facet dependent catalytic efficiency for the selective generation of H_2 from the decomposition of hydrazine. The experimental results suggest that {100} faceted cubic Pd@Ir serves as a better catalyst than those of {111} faceted octahedral Pd@Ir with roughly same size.

2. 3. Metal Oxide Nanoparticles

The recent developments in material science have now shifted to tailor made metal oxides with specific crystal facets to overcome the cost effect of precious noble metal. It has been seen that the exposed facets of oxides nanomaterials tremendously affect the catalytic reaction performance. This provides a new opportunity to understand the nature of active sites and atomic configuration of different crystal facets and the structure reactivity by correlating the reaction property with the exposed crystal facets of oxide nanomaterials.

2. 3. 1. Cuprous Oxides

Cu_2O being a natural product obtained from Earth's crust as cuprites and has attracted engineers and chemist for its p-type semiconducting and catalytic property, especially when

Cu_2O is taken to the nanoregime. Cu_2O has a typical cuprite crystal structure in which body-centered cubic unit cell lattice is built by the copper atoms and oxygen atoms occupy half of the tetrahedral sites.[182] As shown in Fig. 9, all the surface Cu atoms are fully exposed in case of {110} facets, while the {111} facet contains some exposed and some sub-surface Cu atoms. Only partially exposed Cu atoms are available in case of {100} facet of Cu_2O[183] which is also reflected in the experimental results of low reactivity of {100} facet bounded nanocube.

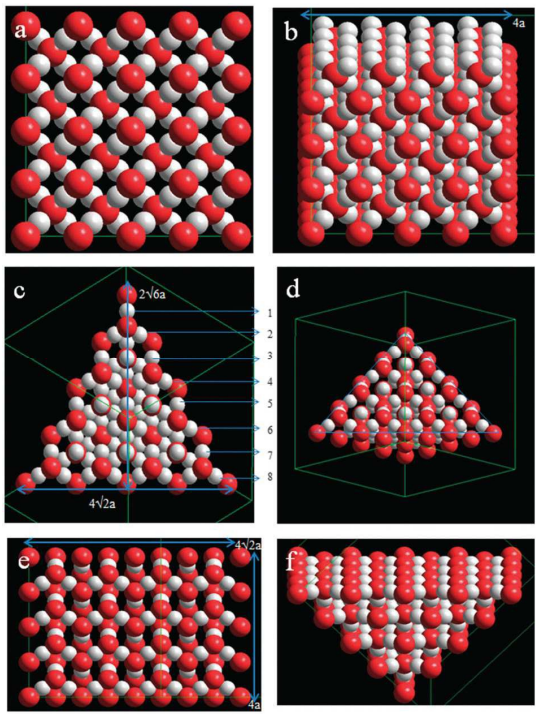

Fig. 9. Crystal structure models of cuprite Cu_2O showing the (a, b) {100}, (c, d) {111}, and (e, f) {110} facets. Oxygen and copper atoms are shown in red color and white color, respectively. Reprinted with permission from ref. 182. Copyright 2013 from Wiley-VCH Verlag GmbH & Co.

Facet dependent catalytic property has recently fascinated scientist to study coupling reaction. It has been shown that {111} faceted octahedral Cu_2O shows higher reactivity towards C-N coupling reaction than {100} facet.[184] As the surface area plays an important role in catalysis, etched products of cube shows improved catalytic coupling reaction.

Recently regioselective catalysis using morphologically different Cu_2O nanocrystals has been reported by Huang *et al*. It was observed that rhombic dodecahedral Cu_2O with {110} facet serves as a best suited catalyst for the regioselective synthesis of 3,5-disubstituted isoxazoles than from {111} faceted octaheral and {100} faceted cubic Cu_2O nanocrystals.[185] In so doing 3,5-disubstituted isoxazoles from a wide variety of aromatic imidoyl chlorides and terminal alkynes in ethanol at 50˚C has been obtained with excellent yields.

Adsorption being the first step in catalysis, many adsorbents has been examined in relation to dye adsorption. There also {111} faceted octahedral Cu_2O nanoparticle serves best leaving aside other morphologically different faceted Cu_2O nanoparticles. [186]

Similarly faceted Cu_2O nanocrystals have been shown to be a good photocatalyst for degradation of negatively charged methyl orange.[187-194]

Huang *et al*. demonstrated facet dependent etching of cubic, octahedral, and rhombic dodecahedral Cu_2O nanoparticles in presence of acetic acid and ammonia solution.[195,196] During etching process, it is observed that {100} facets are more stable whereas less stable {111} and {110} facets are transformed to form new {100} facets.

Hollow 3-D nanostructures of Cu_2O (Fig. 10) are evolved from different faceted solid parental nanostructures capable of scattering visible to near-infrared lights. The preparation procedure takes the advantage of sonnication, etching by HCl and kinetic control through selective expulsion of surfactant molecule.[197]

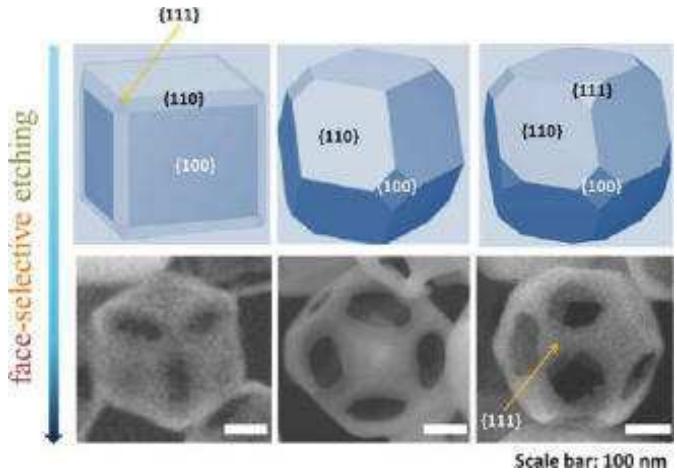

Fig. 10. Facet selective etching of morphologically different Cu_2O nanocrystals. Reprinted with permission from ref. 197. Copyright 2013 from American Chemical Society.

Different surface atomic arrangement of the exposed crystal facets exhibits distinctive antibacterial activity. This was realized by Wang and co-workers introducing E. Coli strain in the reaction medium.[198] From zeta potential measurement, they reported that the electrostatic interaction between E. Coli and {111} faceted octahedral Cu_2O is stronger in inactivating bacteria than from {100} faceted cubic Cu_2O.

The compositional and morphological evolution of differently shaped Cu_2O (octahedron, truncated octahedron, hollow octahedron, cube and sphere) nanoparticles have been studied very recently by introducing different etching agents like aqueous NaOH, triethylamine (TEA) and oxalic acid solution and their oxidative dissolution depends on the exposed crystal planes (Fig. 11).[199] During oxidative dissolution in aqueous oxalic acid solution, it is found that the relative stability of {100} crystal plane is higher than {111} crystal plane. Etching only with oxalic acid exhibits shape transformation from octahedron, truncated octahedron and hollow octahedron Cu_2O nanoparticles to cube and hollow cube as etching products with

50% reduction of edge length. All morphologically different Cu_2O nanoparticles and chemically etched products show facet dependent photocatalytic activity under visible light irradiation. Photocatalytic efficiency of different particles for congo red degradation has shown a close relationship with exposed crystal planes, surface area and particle size. Finally, NaOH etched product with hollow octahedron morphology exposing {111} facets exhibit highest photocatalytic activity.

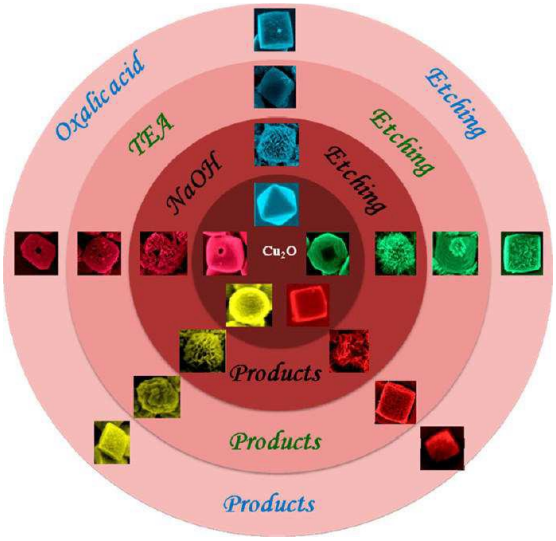

Fig. 11. Chemical etching of morphologically different Cu_2O nanoparticles. Same color of the etched products produced from Cu_2O nanoparticle of a particular shape. Reprinted with permission from ref. 199. Copyright 2013 from American Chemical Society.

In another work Huang *et al*. reported facet dependent electrical conductivity of differently shaped Cu_2O and Au-Cu_2O nanoparticles.[40] The experimental results suggest that {111} faceted octahedral Cu_2O are highly electrical conductive whereas {100} faceted Cu_2O shows

very poor conductivity. Again octahedral Au-Cu_2O core-shell structure shows significant enhancement of conductivity, but cubic Au-Cu_2O core-shell shows little enhancement.

Cu_2O nanocage has been judiciously obtained to encapsulate Au nanorod for possible application. The authors have studied time dependent seed particle growth of two types of Cu_2O nanoframes with variable wall thickness. Slow and faster etching by ethanol and ethanol-HCl mixture in NaOH/SDS solution produced truncated rhombic dodecahedral structure of Cu_2O.[200] The authors have discussed the importance of Au incorporation in Cu_2O cages. Furthermore anion sensitivity of {111} facet with that of {100} facet of Cu_2O has been compared.

2. 3. 2. Titanium Dioxides

Titania has four polymorphs: rutile, anatase, brookite, and TiO_2(B) based on the 3D arrangements of TiO_6 octahedral unit. Of these phases, rutile is the thermodynamically most stable form in bulk titania, whereas anatase is the most stable one when the size goes below 14 nm.[201] Other two polymorphs [brookite, and TiO_2(B)] are not generally obtained in mineral because they exit in metastable forms. The structural variation in different polymorphs arises mainly due to the different sharing of edges and corners of TiO_6 octahedral unit with the adjacent one (Fig. 12). For the anatase phase, TiO_6 octahedral unit are connected by sharing edges. The rutile phase is built by sharing the corners of TiO_6 octahedral unit along a and b direction but the edges along c direction. In case of brookite, the connectivity of TiO_6 octahedral unit along c direction is similar to that of rutile, but along the a and b directions TiO_6 octahedral units are connected by sharing both the corners and edges.[202] For TiO_2(B), the connectivity of TiO_6 octahedral unit by sharing of edges is similar to that of anatase form but the with a different 3D arrangement that generates a layered structure.[203]

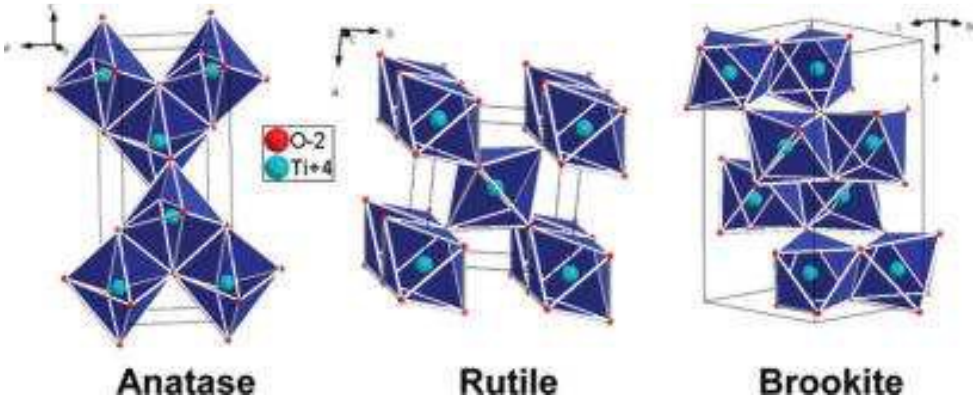

Fig. 12. 3-D Arrangements of the TiO_2 anatase, rutile, and brookite forms. Reprinted with permission from ref. 202. Copyright 2010 from American Chemical Society.

Both {110} and {101} surfaces of rutile and anatase phase are terminated by sixfold- and fivefold- coordinated Ti atoms and threefold- and twofold- coordinated O atoms (Fig. 13).[204] Due to slight orthorhombic distortion, anatase phase is less symmetrical than rutile phase and it also found that the Ti-Ti bond distance is shorter in the anatase form than the rutile form. As a result, anatase TiO_2 becomes less dense and stable than the rutile form due to presence of the degree of distortion in the basic building block. The different exposed crystal facet of TiO_2 is the promoter of heterogeneous catalysis.

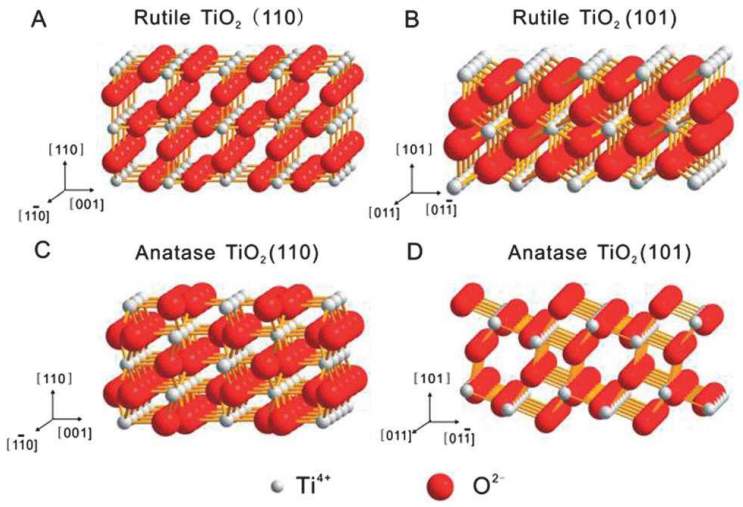

Fig. 13. Atomic configurations of the {110} and {101} crystal facets for anatase and rutile TiO_2, respectively. Reprinted with permission from ref. 204. Copyright 2014 from Royal Society of Chemistry.

TiO_2 nanocrystals are considered by far to be the best catalyst for UV assisted chemical reaction. Recently, TiO_2 nanocrystals with different crystal forms and crystal facets are obtained from hydrothermal reaction involving $Ti(OH)_4$ in presence of anion additives.[205] Restructuring and recrystallization may occur for TiO_2 NCs due to the strong interaction between added anions and TiO_2 surface leading to phase transformation from anatase to rutile or brookite. 'Hard' donor atoms bind differently with the crystal facets of TiO_2 and cause surface restructuring and recrystallization. It has been observed that truncated octahedral anatase TiO_2 NC was obtained when F^- was used as capping anions. F^- is selectively adsorbed on {001} facets of TiO_2 and lower the surface energy, leading to larger percentage of {001} facets. But SO_4^{2-} or Ac^- (acetate ion) in place of F^- upon hydrothermolysis produces anatase TiO_2 nanorods. Longer nanorods are obtained with SO_4^{2-} and short nanorods with Ac^-. Selective photocatalytic reduction of nitrobenzene and selective oxidation of benzyl alcohol

have been elucidated with the different faceted TiO_2 NCs. Comparative accounts of facet selective reactions have been documented for benzyl alcohol oxidation without any facet discrimination but nitroaromatics describe a definitive order of reduction rates of nitrobenzene which follows {101} > {001} > {100} (Fig. 14).

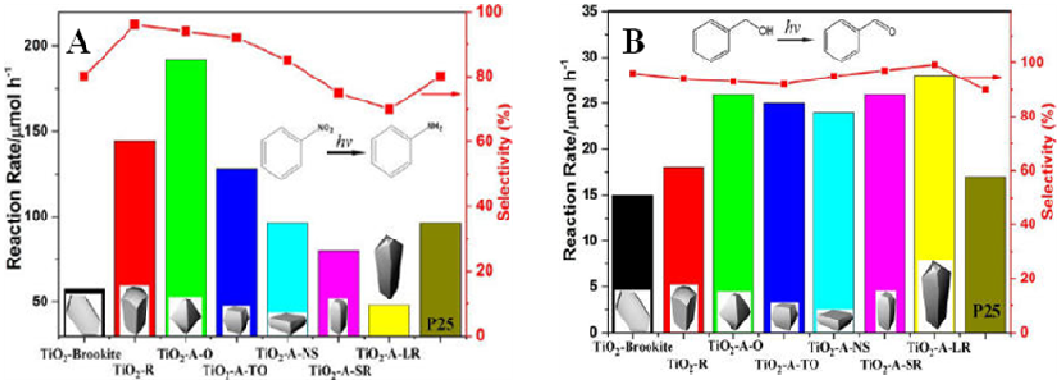

Fig. 14. Photocatalytic performances of TiO_2 nanocrystals with different crystal facets in (A) reduction of nitrobenzene to aniline after reaction for 30 min and (B) oxidation of benzyl alcohol to benzaldehyde after reaction for 4 h. Reprinted with permission from ref. 205. Copyright 2013 from American Chemical Society.

It has recently been discovered that naturally occurring TiO_2 nanocrystals bear energetically favourable {101} facets.[206-209] Furthermore, morphology of the anatase phase represents octahedral bipyramidal structures. It is very difficult to produce TiO_2 nanocrystal with reactive and energetically unfavourable {001} facets. Recently Li *et al*. has discovered a hydrothermal process to stabilize {001} faceted anatase TiO_2 nanosheets in aqueous medium.[210] There F^- ion capping capability has been discussed which promotes oriented attachment along {001} facet via hydrolytic path way. They have also shown that solvents

like HCl, ethanol, propanol, and butanol suppress the hydrolysis of surface Ti-F which helps the retention of original nanosheet morphology.

Recently, Pradhan *et al*. reported the photocatalytic efficacy of anatase TiO_2 nanocrystals.[211] The size dependent TiO_2 nanocrystals have been found to evolve by varying the reaction time. The paper has documented the use of effective diethanolammine capping for {101} facets instead of {100} facets. Thus with increasing reaction time nanocrystals with {101} facets predominates and as a result cuboid nanocrystals are produced with selected facets (Fig. 15). The author has identified high energy oxidative {001} facets and low energy {101} reductive facets. The popular belief of hole-electron pair generation and subsequent decrease of charge recombination have been envisaged in the paper. Finally, TiO_2 nanocrystal with {001} or {100/010} and {101} facets exhibited facet selective photocatalytic activity.

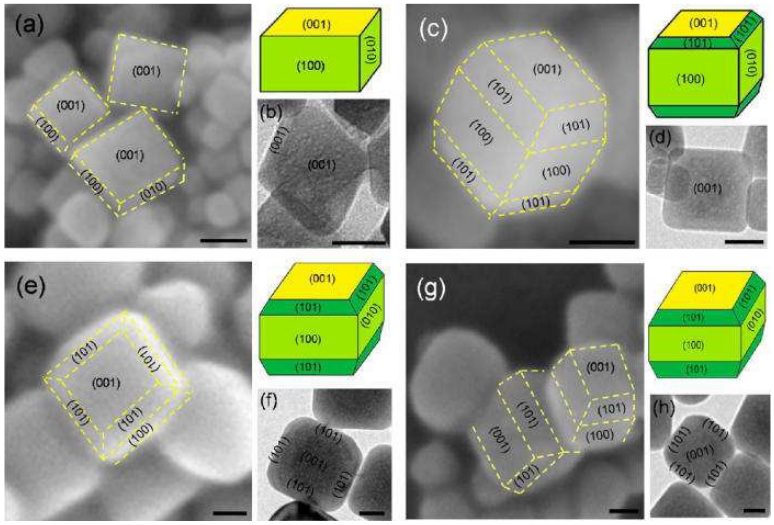

Fig. 15. FESEM, TEM images, and 3-D geometrical models of respective TiO_2 nanoparticles are shown with different facets hydrothermally synthesized in (a, b) 12 h, (c, d) 24 h, (e, f) 36 h, and (g, h) 48 h. The scale bar in all the images is 25 nm. Reprinted with permission from ref. 211. Copyright 2013 from American Chemical Society.

Chen *et al*. reported the photocatalytic efficiency of {001} faceted TiO_2 nanocrystal through both experiment and theory. It has been found that postannealing TiO_2 nanoparticles at 350, 450, and 550 °C exhibited outstanding performance of photocatalytic H_2 production as compared to that of commercial P25. In this report, the enhanced photocatalytic activity of 450 °C calcined sample has been explained by synergistic effect.[212] They have brought in the co-existence of low index faceted structures having dominant {010} and {001} facets which they have termed as quasi hetero-junction. Photocatalytic H_2 evolution by the TiO_2 semiconductor nanoparticle has also been supported by density functional theory.

TiO_2 nanocrystal with uncommon high energy {111} facets has been synthesized by wet chemical synthesis at room temperature. Ye *et al*. have not only synthesized the TiO_2 nanocrystal using F^- and ammonia as capping agents but also substantiated the energetic of high energy faceted {111} structure through density functional theory.[213] The electronic band structure of the {111} faceted TiO_2 nanocrystal is supportive for the generation of more reductive electrons. The authors have proposed high solar energy conversion efficiency from the as-synthesized product with {111} facet than the common faceted anatase TiO_2 nanocrystals with {001}, {010}, {101} facets.

Again faceted TiO_2 nanocrystal has been produced from titanium isopropoxide in acid medium (HF and HCl) under prolong hydrothermal heating using an autoclave.[214] To promote photocatalytic activity of TiO_2 nanocrystals different metallic co-catalysts have been deposited onto the TiO_2 facets to examine facet selective oxidation of glycerol. It has been concluded that {110} facet shows maximum photocatalytic activity while {001} facet performs badly. Intermediate activity has been documented by {101} facet to produce hydroxyl acetaldehyde (HAA).

To make TiO_2 an efficient catalyst many attempts have been made. Among them tuning of the band gap value of TiO_2 by changing its morphology is a fruitful way to improve the

catalytic activity of TiO_2. Furthermore doping of elements is also responsible for tuning the band gap value.[215] Sometimes deposited metals change the catalytic property of the composites drastically. In this regard Haruta's work is a ground breaking one.[216] Here we present one elegant application of Au-TiO_2 composite materials for photocatalytic hydrogen generation.[217] Faceted Au nanoparticles have been deposited onto the high exposed {001} facet of TiO_2. It has been shown that anchored Au{111} shows highest reactivity over the other two [Au{100/111} and Au{100}] Au nanoparticle.

Oxidation of CO has been reported taking faceted TiO_2-Au as the catalyst.[218] In this work faceted TiO_2 has been prepared to host Au nanoparticle. It is clearly shown that reactivity of differently faceted TiO_2 varies with temperature for CO oxidation. Interestingly 100% oxidation has been reported on {100} TiO_2 facet at 253 K with the increasing temperature {001} facet become increasingly important for CO oxidation. At the intermediate temperature i.e.; at 273 K {101} facet converts CO into CO_2 quantitatively.

TiO_2 nanocrystals become activated under UV irradiation and can be best physically modified by a suitable dye. That provides improved visible light photocatalytic activity. Further improvement is governed by noble metal loading on dye-sensitized TiO_2 nanocrystal. This is because of the suppression of charge recombination process. Lu *et al*. loaded Pt onto commercially available P25 Degussa TiO_2 nanocrystals for water reduction.[219] In their report they have explained the improved photocatalytic activity of the composite nanomaterials taking the Fermi level of Pt {111} facets into consideration. In fact neat Pt {111} facet stands active due to larger number of unsaturated Pt atoms at the corners and edges of Pt{111} nanoparticles. Again the position of the Fermi level traps the electron easily out of conduction band of TiO_2. Thus the composite Pt{111}/TiO_2 provides more reaction sites for water reduction than the other two Pt{100/111}/TiO_2 and Pt{100}/TiO_2 nanocomposites.

2. 3. 3. Ferric Oxides

Generally, it is known that four types of Fe_2O_3 polymorphs exist depending upon the atomic arrangements of Fe^{+3} and O^{2-} ions and they are α-, β-, γ-, and ε- phases. Among them highly crystalline α-, and γ-Fe_2O_3 have been studied for a long time due to their nontoxicity, environmental friendliness and abundance in nature. α-Fe_2O_3 has corundum-type structure ($R\bar{3}c$ space group, a = 0.50352 and c = 1.37508 nm) with hexagonal close-packed array of O^{2-} ions, and Fe^{3+} ions occupy 2/3 of the octahedral sites.[220] Whereas γ-Fe_2O_3 has cubic structure ($Fd\bar{3}m$ space group, lattice constant value 0.83474 nm) in which the Fe^{3+} ions are distributed in the tetrahedral (eight Fe ions per unit cell) and octahedral sites (the remaining Fe ions and vacancies) confined by the cubic close-packed array of oxygen anions.[221] Fig. 16 shows the surface atomic configurations of the crystal facets for α- and γ-Fe_2O_3. It is observed that {001} facet is the most frequently exposed facet for α-Fe_2O_3 , which is only terminated by Fe or O atoms, whereas another low-index facet, {100}, simultaneously contains both Fe and O atoms.[222] γ-Fe_2O_3 generally bound by polar and unstable low-index {001}, {011}, and {111} facets and the surface energies of {001}, {011}, {112}, and {012} facets after surface reconstruction are almost equivalent.[223] The catalytic reactivity of Fe_2O_3 depends not only on their crystal phase but also on the exposed crystal facets.

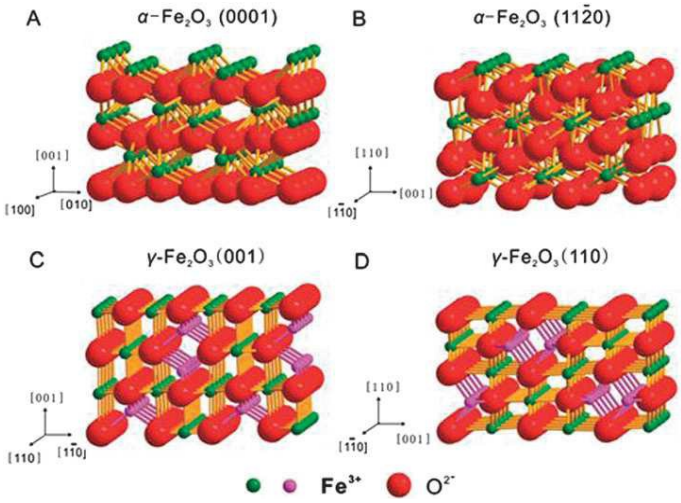

Fig. 16. Atomic configurations of the {0001} and {11$\bar{2}$0} facets for α-Fe_2O_3 and {001} and {110} facets for γ-Fe_2O_3. Reprinted with permission from ref. 204. Copyright 2014 from Royal Society of Chemistry.

Recently Fe_2O_3 has been actively considered as an anode material for lithium storage owing to its high theoretical capacity (1000 mA h g^{-1}). Yu *et al*. reported an interesting flame pyrolysis method for synthesis of 26-faceted truncated cuboctahedral γ-Fe_2O_3 by direct burning of ferrocene in different solvents using an alcohol lamp.[224] The choice of solvents is therefore very important for fabrication of maghemite nanocrystals and their carbon composites. Polyhedron γ-Fe_2O_3 obtained when methanol, ethanol and dimethylformamide were used as solvent, whereas isopropanol, butanol and tetrahydrofuran produced smaller iron oxide nanocrystals encapsulated in carbon. Details mechanism for shape evolution from 14-faceted truncated octahedrons to 26-faceted truncated cuboctahedrons has also been discussed clearly. Fig. 17 indicates that hexagons {111} (indicated as A, B, C, and D) grew faster in truncated octahedron[225] which resulted in the formation of new squares {110} (indicated as O′) and at the same time originally square {100} (marked as O) transformed to octagonal {100} plane (indicated as P) as the surface energies of different facets are different.

It is observed that the surface energies follow the order of σ{101} > σ{001} > σ{111}. From the electrochemical performance of the as-synthesized catalysts as an anode material for Li-ion battery, it can be concluded that γ-Fe_2O_3@C displayed high discharge specific capacity (1050 mA h g^{-1}) and stability than from bare maghemite mainly due to the high electronic conductivity of carbon.

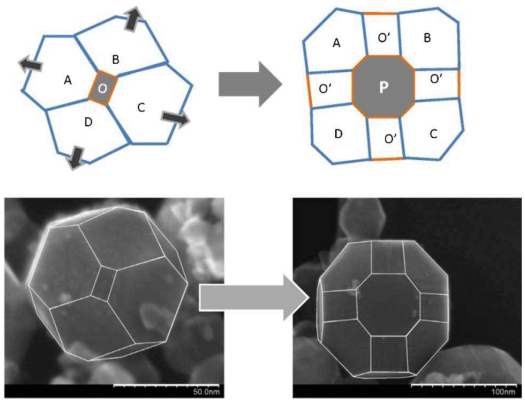

Fig. 17. Cartoon illustration of the formation of truncated cuboctahedrons by further growth of truncated octahedron nanocrystals in the flame. Reprinted with permission from ref. 224. Copyright 2012 from Royal Society of Chemistry.

Shen *et al.* fabricated hexagonal α-Fe_2O_3 nanoplates enclosed by two larger {0001} basal surfaces, which gave higher discharge capacity (1630 mA h g^{-1}) and more cycling stability for Li-ion battery than from a thicker α-Fe_2O_3 nanograins (1510 mA h g^{-1}) enclosed by a variety of crystal facets although both nanocrystals have identical surface area (22.02 and 24.32 m^2 g^{-1}).[226] The better electrochemical performance of hexagonal α-Fe_2O_3 nanoplates is attributed to the presence of significantly larger {0001} planes, shorter thickness along the <0001> direction.

By using solvothermal method Li and the co-workers synthesized 27 nm thick Fe_2O_3 nanodisks bound by {001} facets.[227] By comparing the packing density of Fe^{3+} and O^{2-} for

{001}, {100} and {010} facets (Table 1), it should be clearly concluded that that the packing of O^{2-} in the {001} facet is exactly hexagonal close packing (hcp) but in other two cases packing is not in the manner of hcp (Fig. 18). That is why in the oriented growth of hematite nanodisks, this {001} facet is the most stable and most exposed. In this work the most stable {001} facet of Fe_2O_3 was preserved mainly due to the preferential capping effect of acetate ion. The as-synthesized materials showed excellent rate and cyclic capability as an anode material of Li-ion battery due to reduced diffusion length of Li^+ ions.

Table 1. The atomic densities for the {100}, {010} and {001} facets of Fe_2O_3. Reprinted with permission from ref. 227. Copyright 2013 from Royal Society of Chemistry.

Ions	{100}/nm^{-2}	{010}/nm^{-2}	{001}/nm^{-2}
Fe^{3+}	2.89	2.89	9.11
O^{2-}	5.78	5.78	13.8

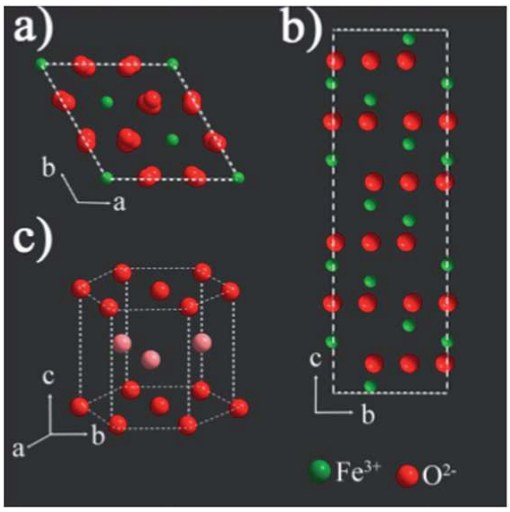

Fig. 18. {001} Plane (a), {100} plane (b) and general view of O^{2-} packing (c) in hematite. The pink balls in (c) correspond to the O^{2-} ions between the top and bottom layers of O^{2-}. Reprinted with permission from ref. 227. Copyright 2013 from Royal Society of Chemistry.

Yan *et al*. investigated the effect of largely exposed {110} facets of hollow sphere like α-Fe_2O_3 for high lithium storage properties and improved photocatalytic activity towards water oxidation.[228] The growth process for formation of three-dimensional hierarchical hollow α-Fe_2O_3 involves three steps. The formation of FeOOH nanosheets on the surface of CuO spheres uniformly occurred in the first stage. In the second stage, core CuO was gradually dissolved in the aqueous solution as $[CuCl_x]^{1-x}$ through etching with in situ produced H^+ ion under hydrothermal condition. As a result, hollow spherical FeOOH was produced. Finally in the last step the products were annealed at 500 ^oC in air and obtained hollow sphere like α-Fe_2O_3 without any structural changes. Due to higher density of Fe atoms on {110} facets of α-Fe_2O_3, the product showed superior Li ion storage performance and enhanced photocatalytic activity towards CO oxidation.

Morphologically different Fe_2O_3 nanoparticles with different dominant facets have also been used in photocatalysis. Layered α-Fe_2O_3 nanodisks have been judiciously obtained through a low cost silicate-anion-assisted hydrothermal method.[229] It is found that silicate ions adsorbed very strongly onto the {0001} facets of α-Fe_2O_3 nanoplates, resulting in a novel layer-by-layer oriented attachment of the nanoplates. So, here silicate ions played a crucial role for formation of such type of rare layered structure of α-Fe_2O_3. In this study, the layered α-Fe_2O_3 showed better photocatalytic degradation activity for methylene blue compared to nanoplates which is mainly due to the higher adsorption capacity of the layered structure.

Rhodamine B degradation on Fe_2O_3 nanoparticle has been studied spectrophotometrically by Chen *et al*.[230] A comparative account of facet selectivity has been underlined in their report in the light of higher density of surface Fe ions on {10$\bar{1}$2} facet. The nanocrystals bearing {0001} and {10$\bar{1}$0} facets with lower density of Fe ions photodegrade the dye less effectively.

Cao and co-workers compared the photocatalytic activity of α-Fe_2O_3 polyhedrons, rods, ellipses, and cylinders bound by different facets for the degradation of organic contaminants in presence of H_2O_2.[231] The photocatalytic performance of differently shaped α-Fe_2O_3 towards methylene blue degradation follows the order: polyhedrons bound by {101} and {001} facet > rods bound by {001} > ellipses > cylinders and the order was not in good agreement with the BET surface area values. The improved photocatalytic activity of polyhedral α-Fe_2O_3 can be ascribed to its higher density of {101} facet.

The study of facet dependent catalytic activity of differently shaped α-Fe_2O_3 nanostructures for heavy metal determination by stripping voltammetry was conducted by Huang and co-workers.[232] They compared the selectivity and sensitivity of Pb^{2+} ion detection by using three types of α-Fe_2O_3 nanostructures including nanocubes, nanoplates, and nanorods with dominant facets of {012}, {001}, and {110}, respectively. {110} facet bound α-Fe_2O_3 nanorods were found to be more active catalyst for Pb^{2+} ion detection and the electrochemical sensitivity is about 6-fold and 32-fold than that of nanoplates and nanocubes. This experimental result is closely related to the DFT calculations.

26 faceted γ-Fe_2O_3 enclosed by six {100}, eight {111}, and twelve {110} facets have been successfully prepared by Gao *et al*. via flame synthesis method by directly combusting the methanolic solution of iron precursor.[233] Then they investigated the catalytic activity of polyhedral γ-Fe_2O_3 for styrene to benzaldehyde conversion reaction compared to other two commercial γ-Fe_2O_3 samples. The catalysis experiment indicates that the 26 faceted polyhedral γ-Fe_2O_3 hold great promise for styrene to benzaldehyde conversion with very high catalytic selectivity because of the large number of different facets, especially the {110} facets which have more number of Fe atoms than {100} and {111} facets in γ-Fe_2O_3.

Faceted α-Fe_2O_3 have also played major role for enhancing gas sensing property. Zheng *et al*. investigated that exposed {110} facets of plate like α-Fe_2O_3 have significant role in acetone

sensing and CO oxidation.[234] They reported a controlled solvent evaporation process for fabrication of porous plate like α-Fe_2O_3 in presence of an ionic liquid [Bmim]Cl which acted as both solvent and templating agent. This nanoplate-like α-Fe_2O_3-400 (annealing at 400˚ C) had higher sensitivity towards acetone than commercial α-Fe_2O_3 which can be attributed to its unique plate-like morphology and its higher crystallinity. Then they deposited different percentage of Au onto the porous plate like α-Fe_2O_3 and tested their catalytic improvement towards CO oxidation. For the same loading of Au on the α-Fe_2O_3 support, {110} faceted α-Fe_2O_3 exhibited superior catalytic activity towards CO oxidation than α-Fe_2O_3 (Fluka).

2. 3. 4. Cobalt Oxides

The structure of Co_3O_4 is usually considered to be spinel ($Fd\bar{3}m$ space group and unit-cell length of 0.8084 nm) and is built by the cubic close packed array of O^{2-} ions and Co^{2+} ions occupy one-eighth of the tetrahedral sites whereas Co^{3+} occupy half of the octahedral sites (Fig. 19). Under equilibrium condition, Co_3O_4 naturally exists with a morphology of a truncated octahedron enclosed by energetically favourable the {001} and {111} faces than the more reactive {110} facets.[235] In addition the reactive {110} facets of Co_3O_4 have two types of surface terminations: in type A two Co^{2+} cations are distributed in the tetrahedral sites, two Co^{3+} cations in the octahedral sites, and four O^{2-} anions; and in type B two Co^{3+} cations are distributed in the octahedral sites and four O^{2-} anions.[236]

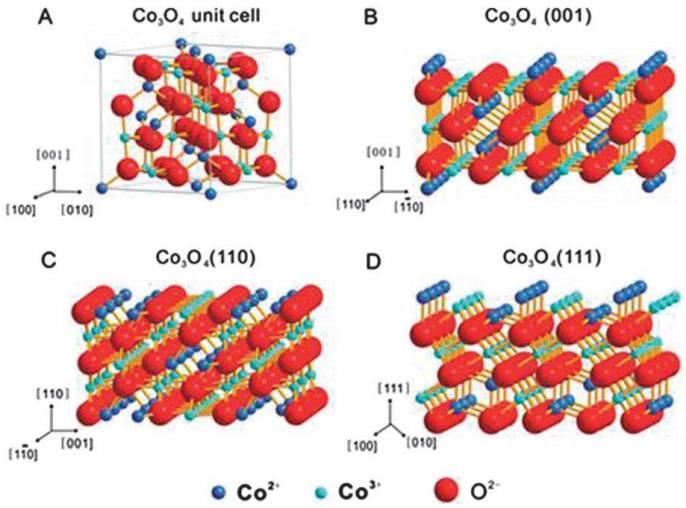

Fig. 19. Atomic configurations of the {001}, {111} and {110} facets for spinel Co_3O_4. Reprinted with permission from ref. 204. Copyright 2014 from Royal Society of Chemistry.

Several strategies have been proposed for synthesis of differently shaped Co_3O_4 nanoparticles bound by different facets for different applications. Facet dependent electroanalytical sensing of heavy metal ions from solution has been described by Huang *et al*. Nanocrystals of Co_3O_4 with two different predominant facets {111} and {001} have been shown to carry different degree of heavy metal ion loading and that is the basis of sensing applications.[237] The hydrolysis of $Co(CH_3COO)_2.4H_2O$ under hydrothermal condition with and without ethylene glycol evolves Co_3O_4 with {111} faceted nanoplates and {001} faceted nanocubes respectively. Theoretical (DFT) calculations suggest that Co_3O_4 {111} facets exhibit a relative larger adsorption energy, more adsorption sites, and a relative lower transition-state barrier than Co_3O_4 {001} facets. This result becomes supportive to the experimental observation for accounting facet-dependent electrochemical sensing behaviour toward heavy metal ions.

Kodambaka *et al*. proposed a simple wet chemical approach for fabrication of single crystalline {111} faceted Co_3O_4 holey nanosheets.[238] Co_3O_4 holey nanosheets exhibited efficient catalytically active for methanol decomposition at low temperature due to presence of higher energy {111} surfaces.

Li *et al*. found that the exposed facets of Co_3O_4 nanostructures including a cube with {001} facet, a truncated octahedron with {001} and {111} facets and octahedron with {111} facet, have a noteworthy influence on their electrochemical performance.[239] Only by changing the amount of NaOH and $Co(NO_3)_2.6H_2O$, they have successfully prepared Co_3O_4 nanoparticles with different facets under hydrothermal condition. When these three materials were evaluated for lithium storage properties, octahedral Co_3O_4 with dominant {111} facets exhibited much better lithium storage capability (946 mAh g^{-1} at a rate of 100 mAh g^{-1} after 50 cycles) than the other two kinds of Co_3O_4. From the surface atomic configuration (Fig. 20) it is observed that {001} plane contains 2 Co^{2+} whereas {111} plane contains 3.75 Co^{2+}, that means {111} plane has more Co^{2+} ions. This data is also in good agreement with the prediction that the lithium storage capacity is greatly facilitated through the exposed {111} facet of Co_3O_4 nanoparticles.

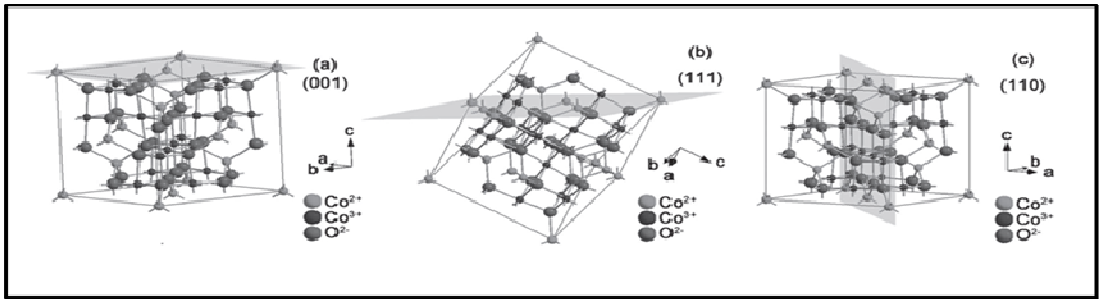

Fig. 20. The surface atomic configurations of the {001} facet (a), {111} facet (b), and {110} facet (c) for Co_3O_4 . Reprinted with permission from ref. 239. Copyright 2012 from Wiley-VCH Verlag GmbH & Co.

Golberg *et al*. have proposed a facile one-step solution approach to obtain unusual single-crystal Co_3O_4 nanocages with highly exposed {110} facets.[240] Clearly the sample showed enhanced lithium storage capacity of 864 mAh g^{-1} at 0.2 C over 50 cycles and excellent rate capability. These improved electrochemical energy storage properties can be attributed to their highly exposed {110} facets, high density of atomic steps on the nanocage surfaces and the large void interiors.

Nie *et al*. synthesized thermodynamically stable {111} Co_3O_4 nanofilms by a microwave-assisted method and subsequent liquid nitrogen cooling using sodium hydroxide and cobalt sulfate solution.[241] During the growth process, liquid nitrogen cooling treatment played a vital role for further aggregation of nanosheets to form nanofilms with high surface area. This {111} faceted Co_3O_4 nanofilms were used as active catalyst for the decomposition of ammonium perchlorate (AP).

2. 3. 5. Nickel Oxides

NiO has a cubic rock-salt crystal structure (Fm-3m) with octahedral Ni(II) and O^{2-} sites. Being a p-type semiconductor, NiO is one of the most promising metal oxide (band gap energy 3.6-4.0 eV) exploited in photocatalysis, electrochemistry, and electrochromics.[242-245]

By using a simple wet chemical approach, Richards *et al*. demonstrated the fabrication of {111} faceted NiO nanosheets with hexagonal holes without adding any template or halide ions for the first time. NiO nanosheets with controllable sizes from 300 nm to 3 μm were synthesized by adjusting the amount of urea while the size of the holes was determined by calcinations conditions.[246] Experimental results suggested that {111} faceted NiO nanosheets with unusual surface were very much active for low temperature methanol decomposition than from conventionally prepared CP-NiO which could be attributed to the high surface energy of {111} facets. In another work, Richards *et al*. proposed that {111} faceted NiO nanosheets with hexagonal holes were also very much efficient adsorbent for the removal of

different dyes (brilliant red X-3B, congo red and fuchsin acid) from aqueous solution than nickel oxide powder (CP-NiO) obtained from conventional thermal decomposition of nickel nitrate.[247]

Mesoporous NiO nanomaterials have been prepared for useful lithium ion storage from wet chemical technique. It has been demonstrated that {110} facet is most reactive which lead to efficient ultrafast lithium storage,[248] which mimics the high power delivery of supercapacitors just like anatase {001} exposed TiO_2 nanosheets.

2. 3. 6. Magnesium Oxides

As illustrated in Fig. 21, {100} facet of MgO is unambiguously the most stable due to its low surface energy. Whereas, in {111} faceted MgO nanocrystals, polar monolayer of oxygen anions and magnesium cations are present alternatively and thus a strong electrostatic field is produced perpendicular to the {111} facet. So fabrication of MgO nanocrystals with highly reactive {111} facets is highly desirable for different applications. Numerous studies have focused on elucidating the relationship between surface structure and surface reaction.

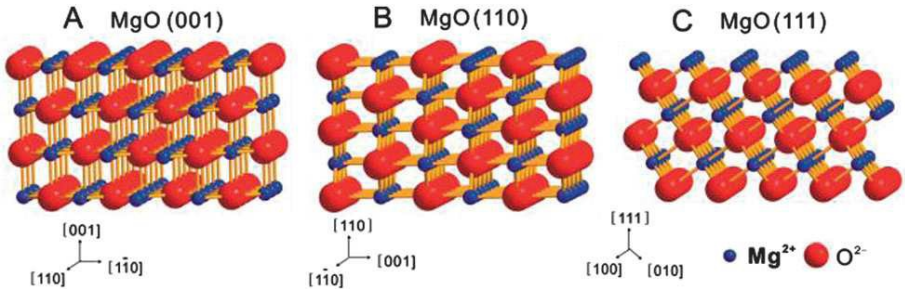

Fig. 21. Surface atomic configurations of the {001}, {110}, and {111} crystal facets for MgO. Reprinted with permission from ref. 204. Copyright 2014 from Royal Society of Chemistry.

When $Mg(OCH_3)_2$ was utilized as a precursor in presence of 4-nitro- or 4-methoxybenzyl alcohol, MgO nanosheets bound by {111} facets were produced preferentially under hydrothermal condition. During the formation of MgO nanosheets, 4-nitro- or 4-methoxybenzyl alcohol played an important role due to their strong interaction with the hydroxyl group of the inorganic intermediate $Mg(OH)(OCH_3)$ which facilitates the spontaneous substitution on the interface during mixing and supercritical treatment. The catalytic activity towards Claisen-Schmidt condensation of benzaldehyde and acetophenone was found to be superior for {111} faceted MgO nanosheets than other MgO samples exposing {100} facets.[249] In 2007, Richards *et al*. further used the {111} faceted MgO nanosheets as an active catalyst for decomposition of methanol at low temperature due to the higher concentration of oxygen anions on the surface of MgO{111} nanosheets.[250]

Again MgO particles bound by {111}, and {100} facets were much more selective during the oxidative coupling of methane to hydrocarbons than cubic MgO.[251,252]

2. 3. 7. Zinc Oxides

ZnO has a stable hexagonal wurzite structure[253-255] in which each O^{2-} ion is tetrahedrally coordinated with four Zn^{+2} ions along the crystallographic c-axis and vice versa.[256] Recently Diebold *et al*.[257] reported that the surface morphology of wurzite ZnO is bound by five low miller index planes: the non polar prism $\{10\bar{1}0\}$ and $\{11\bar{2}0\}$ facets as well as the polar $\{000\bar{1}\}$, {0001}, and $\{11\bar{2}1\}$ facets by using high resolution scanning tunnelling microscopy (STM). During the formation of ZnO nanobelts, nanowires, and nanorods, $\{10\bar{1}0\}$ and $\{2\bar{1}\bar{1}0\}$ facets are appeared as the major facets as the nanostructures grow along <0001> direction.[258,259] $\{10\bar{1}0\}$ facet of ZnO becomes most stable because of its low surface energy value (2.3 J/m^2) and this value is smaller than ZnO$\{2\bar{1}\bar{1}0\}$ (2.5 J/m^2) and those of polar ZnO{0001}-Zn and ZnO$\{10\bar{1}0\}$-O (4.0 J/m^2).[260-263]

Facet dependent gas sensing property of ZnO nanoparticle has been discussed by different groups. By using simple dip-coating method, Xie *et al* synthesized {10-10} faceted ZnO nanorods aligned along the ceramic tube.[264] Then the tube with ZnO thin film was dipped into the growth solution containing zinc acetate and ethylenediamine for formation of further nanorod arrays with {0001} and {10-10} facets (Fig. 22). On the basis of the gas sensing performance, it is observed that the {0001} faceted ZnO nanorod arrays demonstrated excellent catalytic activity towards benzene and ethanol sensing than the unprocessed dip-coated ZnO, which should be explained in the light of exposed facets rather than size effect. So the experimental results suggested that {0001} facet of ZnO is more reactive for gas-sensing rather than {10-10} facets.

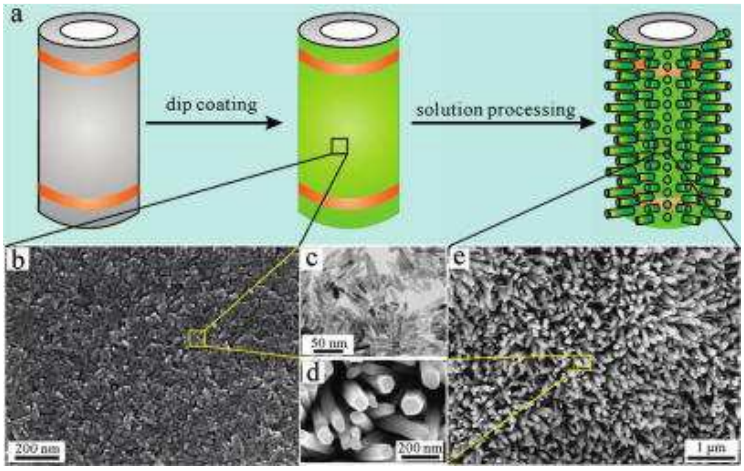

Fig. 22. (a) Schematic representation of the fabrication of solution-processed gas sensor. (b) SEM and (c) TEM images of thin film on the Al_2O_3 tube before the solution process. (d, e) High and low-magnification SEM images of ZnO nanorods array on the Al_2O_3 tube after solution process, respectively. Reprinted with permission from ref. 264. Copyright 2012 from American Chemical Society.

In a same token pronounce gas sensing ability towards NH_3, $N(C_2H_5)_3$, and ethanol vapour has also been tested for {0001} facet of ZnO.[265]

Whereas Yu *et al*. proved that $\{10\bar{1}0\}$ facet of ZnO had excellent sensitivity, selectivity, and stability towards n-butanol than $\{11\bar{2}0\}$, and {0001} facets.[266] In this work, $\{10\bar{1}0\}$ faceted ZnO nanoflakes were synthesized via one-step hydrothermal method. For comparative study, ZnO nanoparticles with $\{11\bar{2}0\}$, and {0001} facets were also employed for sensing capability. The sensing efficiency of different facets towards n-butanol was demonstrated to follow the order of $\{10\bar{1}0\}$ > $\{11\bar{2}0\}$ > {0001} because $\{10\bar{1}0\}$ facet of ZnO had higher adsorption capability and lower diffusion coefficient value. Diffusivity, adsorption, and reaction ability of different gas molecules on different surfaces were elucidate from molecular dynamic (MD) simulations and these findings were closely related to the experimental results. Again this material also showed improved sensitivity towards ethanol, methanol, acetone, and formaldehyde under same experimental condition.

Facet selective CO adsorption has been forwarded on Pd/ZnO surfaces from methanol decomposition studies. Highly active sites Pd/ZnO{0001} have been identified from temperature-programmed experiment leaving aside Pd/ZnO$\{10\bar{1}0\}$.[267]

Facet-selective epitaxial growth of heterogeneous nanostructures of semiconductor (ZnO) has been achieved successfully using faceted noble metal (Ag) nanoparticles.[268] Incoming ZnO nanoparticles were overgrown on {111} facets rather than {100} facets of Ag and produced rod like ZnO nanostructures (Fig. 23). To achieve success lattice and symmetry matching is considered to be the most important factor. Again allowance of direct interfacing between the metal and semiconductor is a corollary factor for over growth which ultimately evolves metal semiconductor hetero-junction.

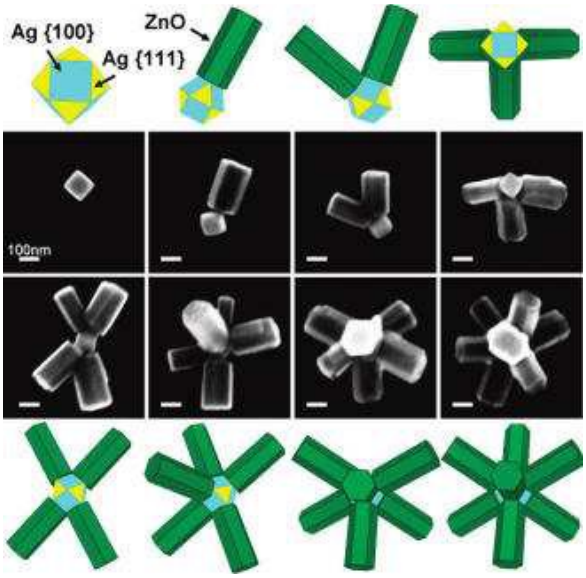

Fig. 23. 3-D Geometrical models and SEM images show the selective growth of different numbers of ZnO nanorods on the {111} facets of Ag truncated nanocubes. Reprinted with permission from ref. 268. Copyright 2009 from American Chemical Society.

2. 3. 8. Tungsten Trioxides

In the temperature range of −180 to 900 °C, WO_3 exhibits five different phases: tetragonal (α-WO_3, > 740 °C), orthorhombic (β-WO_3, 330−740 °C), monoclinic I (γ-WO_3, 17−330 °C), triclinic (δ-WO_3, −43−17 °C), and monoclinic II (ε-WO_3, < −43 °C).[269,270] The generally mentioned WO_3 refers to γ-WO_3 because it is the most stable one at room temperature. Being a p-type semiconductor, γ-WO_3 has attracted noteworthy interest due to its photosensitivity, good electron transport properties, and stability against photo corrosion.[271]

By adjusting the amount of tartaric acid under hydrothermal condition, Wang *et al*. prepared three types of WO_3 nanoparticles with different percentage of {001}, {100}, and {010} facets.[272] Very low amount of tartaric acid was preferentially adsorbed on the top and bottom facets which causes inhibition of growth rate along these facets. As a result a well defined

sheet like structures with thickness of about 30-35 nm were obtained. When the amount of tartaric acid is increased then it adsorbed on the side facets of the WO_3 nanocrystals, resulting in the inhibition of growth along the side facets. So the formation WO_3 nanocrystal with higher thickness (155-175 nm) value was really favoured with high amount of tartaric acid. From the SAED patter it is observed that the WO_3 nanocrystal has three different facets: top and bottom surfaces were bound by {001} facets, and the side surfaces were bound by {010} and {100} facets. Interestingly, the percentages of the different exposed facets in three types WO_3 nanocrystals were different. It should be noted that the percentages of {010} and {100} facets were increased and the percentages of {001} facet was decreased from less thicker sample (1) to high thicker sample (3). Fig. 24 displays that more number of W atoms are present on the {010} facets compared to {100} and {001} facets indicating the presence of more number of dangling bonds in {010} facets. So it should be concluded that the gas sensing ability became more pronounced with increase of {010} facets. Experimental results also proved that WO_3 nanoparticles with exposed more percentage of {010} facets exhibited better gas sensing ability towards 1-butylamine.

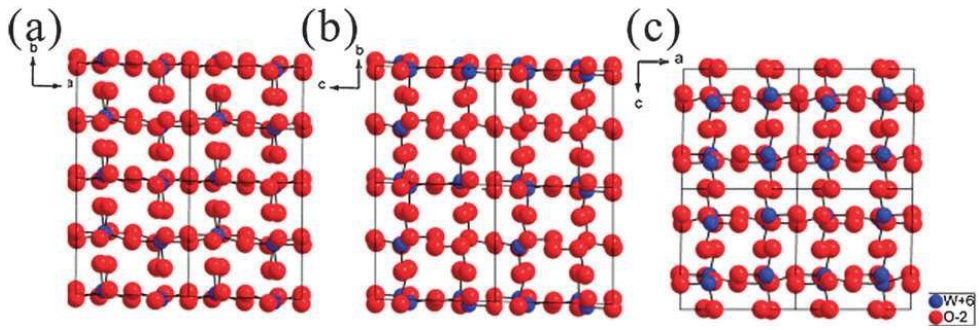

Fig. 24. Surface atomic configuration of different facets for triclinic WO_3: (a) {001} facet, (b) {100} facet, (c) {010} facet. Reprinted with permission from ref. 272. Copyright 2012 from Royal Society of Chemistry.

In 2014, Jin *et al*. also investigated the gas sensing ability of WO_3 nanoparticles with different exposed facets.[273] On the basis of the gas sensing result, it was found that {002} facets of WO_3 nanoparticles showed better acetone sensitivity and selectivity than the {100} facets due to the asymmetric distribution of unsaturated coordinated O atoms in the O-terminated {002} facets. These findings were also supported by the PL spectra which depicted that {002} faceted WO_3 nanoparticles had numerous oxygen vacancies and defects.

Miyauchi invented a new karstification method for preparation of octahedral WO_3 nanoparticles with {111} facets from irregular shaped of commercial WO_3 nanoparticles.[274] During the growth process, commercial WO_3 nanoparticles were etched by ammonia from gradual urea decomposition to produce $(NH_4)_2WO_4$ and this etching process is similar to the Karst process. In the second step, as-prepared $(NH_4)_2WO_4$ was further reacted with HCl and ultimately produced octahedral WO_3 particles in nanoregime. For the formation of {111} faceted octahedral WO_3 nanoparticles, the effect of ethanol in the reaction mixture was undoubtedly significant. Here the presence ethanol in the reaction mixture reduced the polarity of the solvent which inhibited the homogeneous nucleation growth and formed octahedral-shaped particles. The as-synthesized octahedral WO_3 nanoparticles bound by {111} facets showed enhanced catalytic activity for removal of dissolved Ag^+ ions in photoprocessing wastewater as well as visible light driven photocatalytic reducibility of methylene blue dye.

Li *et al*. adopted hydrothermal method for fabrication of hexagonal single crystal WO_3 nanorods with dominant {001} and $\{1\bar{1}0\}$ facets by using $(NH_4)_2WO_4$ as the tungsten precursor in acidic medium.[275] During the formation of hexagonal WO_3 nanorods, it is observed that the crystal growth orientation was sturdily dependent on the tungsten source. NH_4^+ ion of the precursor salt strongly adsorbed on to the {001} facets, resulted in the inhibition of crystal growth along [001] axis. So NH_4^+ ion played a crucial role for initiating

the crystal growth along either [110] axis (Fig. 25). Theoretical model of single crystal WO_3 suggested that, more coordinatively unsaturated W atoms were exposed on the surface of the {001} facets compared with {100} facets. As a result of high surface area and presence of more reactive {001} facets, hexagonal WO_3 nanorods showed high adsorption capacities for organic dyes including rhodamine B and methylene blue.

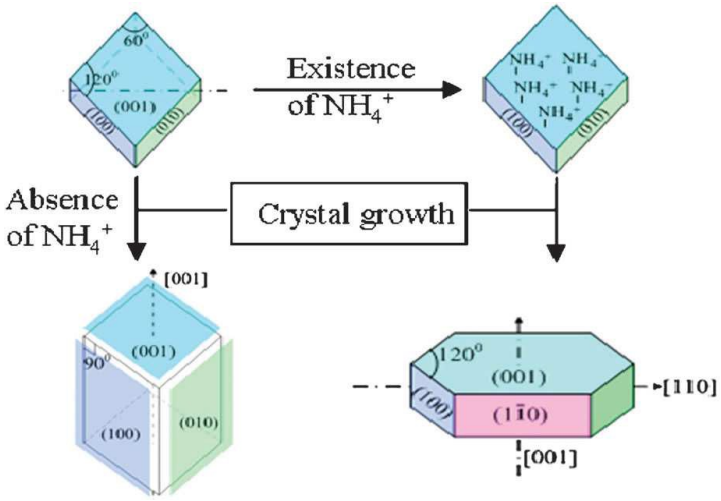

Fig. 25. Schematic representation of the growth orientation of the hexagonal single crystal WO_3 nanorods. Reprinted with permission from ref. 275. Copyright 2011 from Royal Society of Chemistry.

In a combined hydrothermal and finger rubbing method, Kang *et al*. described synthesis of {020} faceted $WO_3.H_2O$ nanoplates using L-ascorbic acid as the capping agent on the surface of fluorine doped tin oxide (FTO) coated glass substrate.[276] After calcination, orthorhombic $WO_3 \cdot H_2O$ nanoplate has been transformed to monoclinic γ-WO_3 with exposed {002} facet without destroying the plate-like structure. Then this {002} facet dominant film has been applied for water splitting reaction. According to previous report, the surface energy order of different facets for monoclinic WO_3 follows the sequence of {002} (1.56 J m^{-2}) > {020}(1.54

J m^{-2}) > {200}(1.43 J m^{-2}) that means the most reactive surface of γ-WO_3 is {002} facet. Because of this feature, {002} faceted γ-WO3 served as a better catalyst for water splitting reaction compared with the WO_3 thin film prepared by spin-coating with same thickness. Quasi-cubic-like WO_3 nanocrystals with equal percentage of {002}, {020}, and {200} facets, prepared by controlling acid hydrolysis of tungsten boride, served as a superior catalyst for solar energy conversion compared with the rectangular sheet-like WO3 nanocrystals with predominant {002} facets.[277]

2. 3. 9. Silver Oxides

Ag_2O has the same cuprite crystal structure like Cu_2O. The etching property of Ag_2O nanoparticle is also facet dependent. Silver nitrate easily reacts with NaOH and produces Ag_2O. On the other hand $AgNO_3$ and even freshly precipitated AgCl dissolves in ammonia forming $Ag(NH_3)_2^{+1}$ complex. Considering the above precipitation and complexation reaction, Huang *et al*. controlled the etching of differently shaped Ag_2O nanacrystals (Ag_2O nanocubes, rhombicuboctahedra, octahedra, and extended hexapods).[36] It has been verified that {100} faceted cubic and rhombicuboctahedral Ag_2O are very much susceptible to etching due to less effective adsorption of hydroxide ions on the {100} facets with terminal oxygen atoms. On the other hand {111} facet of Ag_2O, because of the significant terminal Ag atoms at the corner make the nanocrystal stable because of strong interaction with NaOH. Morphologically different Ag@Ag_2O have been synthesised by kinetically controlled reaction to show the facet selective photocatalytic degradation of methyl orange (MO).[278] Experimentally as well as DFT calculation conclude that highest surface energy bearing {100} facet is the most potent for the photocatalysis of MO. Suitable redox potential driven observation has been explained by the weighted average effective mass of holes and electrons for the reaction.

2. 3. 10. Indium Oxides

Only very recently, researchers have introduced highly conducting and electrochemically stable faceted In_2O_3 nanoparticles for different catalytic applications. For its highly prevalent body-center-cube (bcc) structure with compatible band gap energy, In_2O_3 has proved to be a stable photocatalyst. For the bcc In_2O_3, it is observed that the order of surface energy (γ) for low index facets is as follows: γ {111} < γ {001} < γ {110}. Wu and co-workers investigated the morphological evolution of {001} faceted cubic In_2O_3 nanoparticles by employing a modified chemical vapour deposition method based on the carbothermal reduction reaction.[279] Faceted cubic In_2O_3 are anticipated to show pronounced photoeletrocatalytic activity and excellent chemical and structural stability in oxygen evolution reaction than those with a smaller percentage of the exposed {001} facets. The enhanced catalytic activity of cubic In_2O_3 is mainly due to the unique structure and electronic band structure of {001} facets.

Facet dependent enhanced gas sensing property of octodecahedral In_2O_3 has also been described by Chen *et al*.[280] Octodecahedral In_2O_3 with two different predominant facets {110} and {100} have been successfully synthesized by annealing the 18-facet $In(OH)_3$ precursor. XPS result suggests that In_2O_3 nanoparticle with {110} and {100} facets provides more oxygen vacancy, responsible for pronounced gas sensing property, than {100} faceted cubic In_2O_3 or irregular one.

2. 4. Composite Nanomaterials

Octahedral, cubic, and spherical CuO-MnO_2 nanocomposites have been synthesized by redox transformation reaction between Cu_2O (octahedral, cubic, and spherical) and $KMnO_4$ under modified hydrothermal condition (Fig. 26). Interestingly faceted CuO-MnO_2 nanocomposites are obtained with the retention of parental size and shape of Cu_2O precursor compound. However morphologically different CuO-MnO_2 nanocomposites are found to be ruptured into

tiny spherical nanocomposites with the increase of reaction time. All these composite nanomaterials were employed as catalysts for the examination of facet-dependent catalytic activity toward nitroarene reduction in presence of $NaBH_4$. {111} faceted octahedral CuO-MnO_2 nanocomposites showed higher catalytic efficiency than from cubic and spherical nanocomposites.[281] So the catalytic efficiency for the reduction reaction follows the order of {111} > {100}.

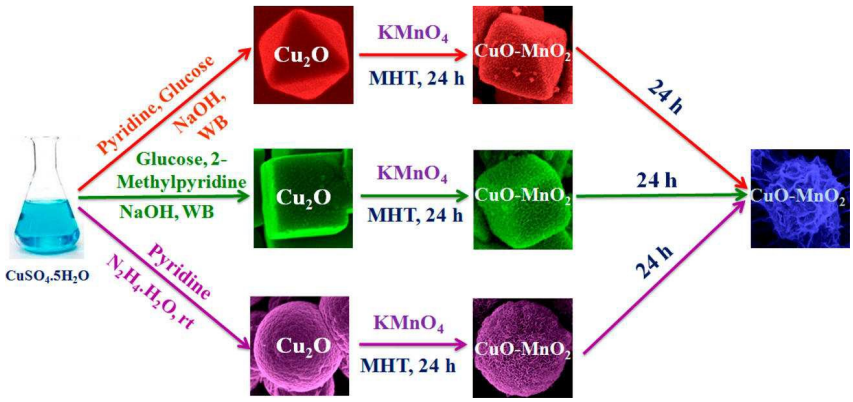

Fig. 26. Schematic illustration of formation of morphologically different CuO−MnO_2 nanocomposites. Reprinted with permission from ref. 281. Copyright 2014 from American Chemical Society.

Facet selective growth of SnO_2 nanorods on the surface of α-Fe_2O_3 has been reported by Yan *et al*. By using {11-20} and {10-10} faceted α-Fe_2O_3 with different morphologies (nanorings, nanocolumns, nanotubes and nanoplatelets) as template, they have synthesized α-Fe_2O_3-SnO_2 composite nanomaterials under hydrothermal condition using $Sn(OH)_6^{2-}$ as the precursor.[282] The preferential growth of SnO_2 nanorods on the {11-20} and {10-10} surface of α-Fe_2O_3 nanotube and nanocolumn along [101] and [101]/[001] directions, respectively have been studied thoroughly by using TEM and HRTEM analysis (Fig. 27). The growth of SnO_2 nanorods on the surface of α-Fe_2O_3 nanoring is similar to that of α-Fe_2O_3 nanocolumn (Fig.

27A). HRTEM image in Fig. 27B indicates that SnO_2 nanorods grow along [001] direction of α-Fe_2O_3 nanoplatelets. The experimental finding of oxygen atomic position on both side of $\{11\text{-}20\}_{\alpha\text{-}Fe2O3}/\{101\}_{SnO2}$ and $\{10\text{-}10\}_{\alpha\text{-}Fe2O3}/\{001\}_{SnO2}$ interfaces suggests slight deviation of oxygen atoms from their original position.

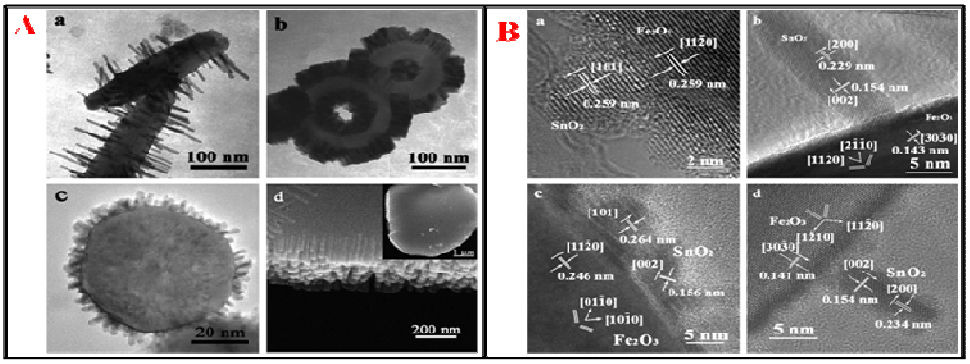

Fig. 27. (A) TEM images of (a) α-Fe_2O_3(nanotube)–SnO_2, (b) α-Fe_2O_3(nanoring)–SnO_2, (c) α-Fe_2O_3(nanocolumn)–SnO_2 composites and (d) SEM images of α-Fe_2O_3(platelet)–SnO_2 composites. (B) HRTEM images of (a) α-Fe_2O_3(nanotube)–SnO_2, (b) α-Fe_2O_3(nanoring)–SnO_2, (c) α-Fe_2O_3(nanocolumn)–SnO_2 and (d) α-Fe_2O_3(platelet)–SnO_2 composites. Reprinted with permission from ref. 282. Copyright 2012 from Royal Society of Chemistry.

3. High Index Faceted Nanomaterials

Recently high index facets (HIFs) have brought new insights for the improvement of facet selective catalytic reactions. High-index facet is generally represented by {hkl} Miller indices in which at least one index greater than unity. Due to presence of high density of low-coordinated atoms, steps, edges and kinks within the structures, metal and metal oxide nanocrystals with high index facet possess more active catalytic sites. According to thermodynamic consideration, such types of facets are absent from the crystals in most of the

cases due to their higher chemical reactivity. So for enhanced catalytic activity, design and fabrication high index faceted metal or metal oxide nanoparticles is now a challenging task. Recent studies shown that high index faceted nanocrystals have been synthesized either by selective overgrowth technique or by site-specific dissolution of nanoparticles. Over the past several years, different synthetic protocols have been developed for synthesis of metallic (Au, Ag, Pt, Pd) and bimetallic nanoparticles with high index facets in order to improve their catalytic or electrocatalytic reactivity. In comparison, preparation of high index faceted oxide nanoparticles and their enhanced catalytic activities is not well explored.

3. 1. Metal and Bimetallic Nanoparticles

Pt concave nanocube enclosed by high index facet including {510}, {720}, and {830} was prepared by using a simple route based on reduction in aqueous solution by using two syringe pumps.[283] Formation of Pt pyrophosphate complex in the reaction mixture and controlled reaction rate by using a syringe pump play crucial role for selective over growth of seeds from corners and edges. At the same time by introducing an additional capping agent KBr in the reaction system, Pt concave nanocube has been obtained by selective capping of {100} facets of seeds. So by using controlled overgrowth technique onto the selected corners or edges and capping of particular facets, it is possible to obtain high index faceted metal nanoparticles. However, these Pt concave nanocubes show a superior electrocatalytic activity towards ORR reaction compared with those of Pt cubes, cuboctahedra, and commercial Pt/C catalysts that are bounded by low-index planes such as {100} and {111}.

Keeping this idea in mind, in 2011 Xia *et al*. have demonstrated pronounced catalytic efficiency of high-index {730} faceted Pd concave nanocubes towards electro-oxidation of formic acid and in the Suzuki coupling reaction leaving aside regular cubes enclosed by low index {100} facets.[67]

In a simple synthetic strategy, Pt concave nanocubes (CNC) have been synthesized by reduction of H_2PtCl_6 in presence of PVP and glycine.[284] Experimental findings suggest that here glycine behaves as size and shape controller by manipulating the reduction kinetics. It is observed that the selective binding of glycine on this high index {hk0} facets of Pt nanocrystals during growth plays a vital role for formation of such type of Pt CNCs. On the other hand PVP has no promising role for formation of Pt CNCs, but absence of PVP causes aggregated products. So by introducing the stabilizing agent PVP in the reaction mixture, dispersed Pt CNCs with {hk0} can be obtained. When this Pt CNC was used as catalyst for electro-oxidation of methanol and formic acid then it is found that Pt CNC serves as a best suited catalyst than commercial Pt black and Pt/C.

Anticipating pronounced plasmonic properties of high-index faceted Au nanocrystal, Han *et al*. reported, for the first time, the synthesis of high-index {321} faceted hexoctahedral Au nanocrystal.[285] By judicious employment of reductant concentration, capping agent and temperature of the reaction they obtained high-index faceted hexoctahedral Au nanocrystal for higher SERS activities leaving aside low index faceted Au nanocrystals.

Using SERS as an experimental tool, Wang *et al*. reported intrinsic facet dependent catalytic efficiency of morphologically different Au nanoparticles enclosed by different types of high-index facets towards hydrogenation reaction of 4-nitrothiophenol at room temperature.[286] They also compared the performance of high-index faceted Au nanocrystals with that of low index faceted Au in the catalysis. There, the order of the catalytic activity is explained by the distribution of coordinatively unsaturated surface atoms on various crystal facets.

In 2015, Wang *et al*. also used surface enhanced Raman scattering as a time-resolved in situ spectroscopic tool to study the facet dependent interfacial molecular transformations on Au nanocatalysts. Using cationic surfactant and suitable reductant in presence of Cu^{+2} ions, they produced high and low index faceted morphologically different Au nanocrystals.[287] In this

work the importance of faceted Au nanocrystals over conventional cylindrical Au nanorods has been described for pronounced optical extinction spectral features, plasmonic tenability and superior catalytic activity towards reduction of 4-nitrophenol.

Considering high surface energy of Rh in comparison to other noble metals, Sun *et al*. could synthesize high-index {830} faceted tetrahexhedral (THH) Rh nanocrystals by employing the electrochemical means. They eventually proved superior electrocatalytic activity of THH Rh nanocrystal over commercial Rh catalysts towards ethanol and CO oxidation.[288]

Huang *et al*. described the relationship between the coordination number of surface Rh atoms and thermal and shape stability of high index faceted Rh nanocrystals by employing molecular dynamic simulation.[289] There from bonding states analysis, it has been concluded that thermal and shape stability of {210} faceted Rh NC is higher than the {310} and {830} faceted ones. This is further explained considering the constitutions of {830} faceted structure which is really composed of {210} and dominant {310} subfacets.

The influence of GO for synthesis of PtPd alloy concave nanocubes with high index facet has been explored by Chen *et al*. for the first time.[290] In absence of GO, reaction mixtures were able to prepare only cubic PtPd alloy. In this present study GO played not only as a catalyst support but also a structure-directing agents for formation of such type of high index faceted alloy. Fig. 28 represents the growth mechanism for formation C-PtPd-RGO. Here small Pd nanocluster should form first on the RGO sheets due to their strong interaction. Then Pt component grew gradually on Pd nanocluster via galvanic replacement reaction, followed by co-reduction of Pt and Pd precursors. Finally the as-synthesized C-PtPd-RGO showed enhanced electrocatalytic activity and high durability toward methanol oxidation due to the presence of high-index {730} facets and the strong interaction between catalysts and graphene support.

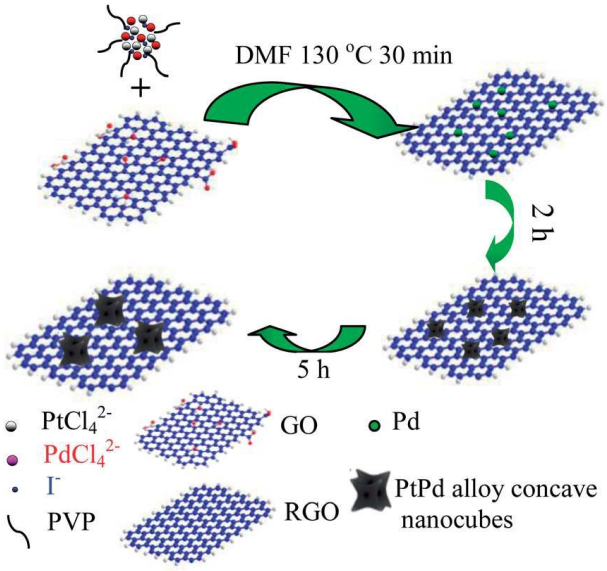

Fig. 28. Schematic representation of the formation of RGO-supported PtPd alloy concave nanocubes. Reprinted with permission from ref. 290. Copyright 2014 from Royal Society of Chemistry.

Yan *et al*. synthesized Pt-Cu and Pt-Pd-Cu concave nanocubes enclosed by {hk0} HIFs through progressive galvanic replacement reaction in a one pot hydrothermal process.[291] Whereas by solvothermal method Li *et al*. prepared high index faceted Pt-Cu concave hexapods.[292] Despite these two synthetic approaches, Yang *et al.* further reported a new but simple oil-phase method for synthesis of concave nanocube like Pt-Cu alloy bound by HIFs.[293] In all the three cases catalysts exhibited enhanced electrocatalytic activity for methanol oxidation reaction due to presence of HIFs.

Another drastic enhancement in catalytic activity towards hydrogenation of styrene arises due to existence of {hk0} HIFs in concave Pt_3Co nanocubes.[294] Such type of unstable structure can be prepared by maintaining an appropriate ratio of oleylamine and oleic acid (Fig. 29).

The superiority of the catalytic activity of Pt_3Co concave nanocube with HIFs can be ascribed due to the presence of more open structure and more active atomic sites.

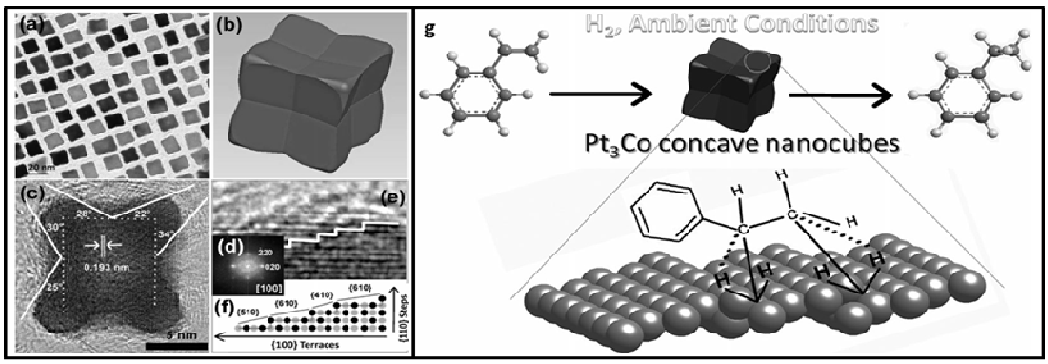

Fig. 29. (a) TEM image, (b) 3-D geometrical model, (c) HRTEM image and (d) Fourier transform pattern of Pt_3Co concave nanocubes. (e) Stepped surface highlighted from the HRTEM image. (g) Schematic representation of Pt_3Co nanocatalyst-involved styrene-hydrogenation reaction. Reprinted with permission from ref. 294. Copyright 2014 from Wiley-VCH Verlag GmbH & Co.

Leung *et al*. reported the fabrication of FeNi concave nanocube with HIFs through one pot, surfactant free electrochemical method by manipulating the growth kinetics of Fe and Ni.[295] In the second steps they developed a new avenue for the synthesis of monodispersed concave nanocage like Fe-Ni with HIFs via a material independent electroleaching process. During electroleaching process it is observed that material dissolution started at the center of the concave face and to the edges continued until the complete cage formation takes place. Due to higher strain and chemical potential, the concave faces are more pronounced for the etching process rather than the edges of the cube. Remarkably, the high index facet exposed concave nanocage and concave nanocube like Fe-Ni showed 100 fold and 10 fold enhancement in the catalytic activity towards electrodetection of 4-aminophnol relative to

cuboctahedrons with convex surfaces. The superiority of the former as catalyst has been explained in terms of high index planes in the cavities of the nanocage and higher active surface area.

3. 2. Metal Oxide Nanoparticles

3. 2. 1. Cuprous Oxides

The applications of Cu_2O nanocrystals enclosed by HIFs have mainly been focused in the field of photocatalysis and CO oxidation. It was found that high index faceted Cu_2O nanocrystals could improve their catalytic efficiency towards these reactions compared with other low index faceted Cu_2O nanocrystals.

Wang and co-workers reported the catalytic activity of polyhedral 50-facet Cu_2O nanoparticle enclosed by high-index {311} facets by maintaining the concentration of OH^- and the volume ratios of polar solvents to water in the mixed solvent for CO oxidation.[296] In another work, concave octahedral Cu_2O microcrystal mainly enclosed by {332} high index facets have been synthesized in presence of an anionic surfactant SDS (sodium dodecyl sulfate) for superior performance in CO oxidation.[297]

Guo *et al*. recently reported a facile one step synthetic method for fabrication of multifaceted Cu_2O that can be considered as an active photocatalyst for reforming glucose under visible light.[86] It was observed that preferential accumulation of photogenerated electrons on high index {104} facets and holes on {100} facets of a Cu_2O polyhedron were responsible for efficient charge separation and as a result Cu_2O with more HIFs showed enhanced photocatalytic activity for reforming of glucose.

Yang *et al*. demonstrated that polyhedral 50-facet Cu_2O nanoparticle enclosed by 24 high-index {211} facets, via a facile seed-mediated solution phase route, showed a much higher photocatalytic activity toward methyl orange degradation than that of the products with low index facets.[298]

Similar photocatalytic improvement towards methyl orange degradation was also achieved in other high index faceted Cu_2O nanocrystals such as {522} facet enclosed polyhedron Cu_2O and {211}, {522} or {311} faceted perfect polyhedral Cu_2O.[299,193,194]

3. 2. 2. Ferric Oxides

Lu *et al*. demonstrated the synthesis of two kinds of brand new high-index faceted polyhedral iron oxide: tetrakaidecahedra and oblique parallelepipeds with the assistance of the viscous macromolecule sodium carboxymethyl cellulose (CMC) and the addition of different amount of N_2H_4 solution.[300] In this work CMC played a key role as stabilizing agent by dividing the solution into numerous channels in the reaction system because it have many carboxymethyl side groups which prohibits them from getting close to each other. Whereas in basis medium (by addition of N_2H_4) Fe_2O_3 grew faster, so by varying amount of N_2H_4 one can controlled the growth of Fe_2O_3 nanoparticle with different exposed surfaces.[301] From magnetic measurements it is observed that two types Fe_2O_3 nanoparticle with different HIFs showed different magnetic behaviour. The tetrakaidecahedral α-Fe_2O_3 bound by {012}, {102}, and {001} facets, might be spin-canted ferromagnetically controlled at room temperature and it disappeared at temperatures lower than T_m (Morin transition temperature) while the other i.e., the oblique parallelepiped α-Fe_2O_3 form bound by {012}, {01-4}, and {-210} facets showed spin-canted and defect ferromagnetism at room temperature.

Similar type of magnetic behaviour was also achieved in other two high index faceted α-Fe_2O_3. Here quasi-cubic α-Fe_2O_3 bound by {012}, {10-2}, and {1-12} facets and hexagonal bipyramid α-Fe_2O_3 polyhedrons with {012} facets have been successfully synthesized only by applying metal ions Zn^{+2} and Cu^{+2}, respectively as structure-directing agents.[302]

Additionally, in 2013 Gao *et al*. reported Ni^{+2} ion induced synthesis of high index faceted α-Fe_2O_3 and their facet-controlled magnetic properties.[303]

Hou *et al*. reported the fabrication of different phase of iron oxides with varied shapes and ultimately the effect of HIFs for photocatalytic degradation of RhB dye.[304] Appropriate ratio of oleylamine and acetylacetone played a key role for formation of different phase of iron oxide (α-Fe_2O_3 and Fe_3O_4) with varied shapes. Here oleyammine provides a strong reductive environment for the reduction of Fe^{+3} to Fe^{+2} and on the other hand acetylacetone affects Fe^{+3} by giving an oxidative atmosphere. Whereas truncated nanocube and oblique nanocube like α-Fe_2O_3 were formed in presence and in absence oleic acid. This experimental finding suggested that oleic acid played an important role in tuning the crystal shape as the carboxylic groups of oleic acid have a strong chelating ability and the non polar tail group behaves as a stabilizing function of this ligand. Truncated nanocube like α-Fe_2O_3 with {102} and {104} facets showed higher photocatalytic activity for degradation of RhB than oblique nanocube like α-Fe_2O_3 with {102} facets due to presence of more active high index facets.

Presently, Yu and co-workers compared the photocatalytic activity of {012} faceted α-Fe_2O_3 nanocubes and {001} faceted α-Fe_2O_3 nanoplates for degradation of methyl orange (MO) and rhodamine B (RhB) under visible light in presence of H_2O_2.[305] From DFT calculation it should be noted that the adsorption energy of MO on {012} and {001} facets of α-Fe_2O_3 is higher than that of RhB and the adsorption energy for MO and RhB on {012} facet is higher than {001} facet. Experimental results also suggested that {012} faceted α-Fe_2O_3 served as a better photocatalyst than {001} faceted α-Fe_2O_3. That means a particular facet on nanoscale has definite selectivity in heterogeneous photocatalysis.

Again the improved photocatalytic activity of truncated nanooctahedral α-Fe_2O_3 with high index {102} facets has been discussed by Gao *et al*.[306]

Zheng and coworkers have followed the routine but systematic change in the concentration of the precursor compound, solvent parameter and reaction time for the synthesis of different faceted Fe_2O_3 nanoparticles.[307] Supersaturation condition has been proved to evolve high

energy {113} faceted Fe_2O_3 nanocrystals whereas {012} or {001} faceted Fe_2O_3 nanocrystals were produced from lower supersaturated condition from hydrothermal synthesis. However, comparatively low energy facet {012} supports better catalytic performance for CO oxidation. For gas sensing {113} facet becomes the best suited one. But least efficiency for both CO oxidation and gas sensing ability was observed for {001} facet.

Tailoring the high index facets of α-Fe_2O_3 could also play a crucial role for gas sensing. One impressive related result is that for a given acetone concentration high index {104} faceted α-Fe_2O_3 shows higher sensor response than from the commercial α-Fe_2O_3 powder.[308] Such type of {104} faceted α-Fe_2O_3 have been synthesized by simple hydrothermal method through an aggregation, phase transformation and recrystallization mechanism. Zhao *et al*. demonstrated that formamide in the reaction mixture plays a pivotal role for synthesis of such type of unstable structure with high reactive facets. Here formamide molecules selectively adsorbed on highly reactive {104} planes, resulting in the preservation of {104} planes. So formamide serves as a facet directing agents.

Wang *et al*. demonstrated polyhedral α-Fe_2O_3 based on oriented attachment growth process in presence of CMC (carboxy methyl cellulose) and PVP, which gave excellent gas sensing selectivity to ethanol vapour due to the exposure of high index facets.[309]

Wu *et al*. studied the influence of double ligand PO_4^{3-} and formamide for formation of HIFs {112} exposed hexagonal α-Fe_2O_3 nanorods.[310] It is found that PO_4^{3-} adsorbs very strongly on the facets parallel to the c-axis restraining the growth along radial direction, while formamide selectively adsorbs on the {112} facets and leads to restrained the growth of α-Fe_2O_3 along {112} direction. Due to presence of high surface energy facets hexagonal α-Fe_2O_3 nanorods show enhanced electrochemical sensing capability toward H_2O_2 ranging from 40 μM to 4.66 mM.

Similar improvement was also achieved in other high indexed octadecahedral α-Fe_2O_3 bound by twelve dominant {112} facets and six {104} facets toward H_2O_2 sensing.[311]

In a recent study, Li *et al*. investigated the catalytic properties of concave nanocube like α-Fe_2O_3 with high index {13$\bar{4}$4} and {12$\bar{3}$8} facets for low temperature CO oxidation.[312] 100 % CO conversion was achieved at 160˚C when HIF exposed α-Fe_2O_3 was used as catalyst. But for α-Fe_2O_3 nanorods CO conversion was only 10.8% though it has higher surface area (39.3 $m^2 g^{-1}$) than form α-Fe_2O_3 nanocube (13.7 $m^2 g^{-1}$). So here the exposed crystal planes play very important role rather than the surface area for determining the catalytic efficiencies of the catalyst. Again this enhanced efficiency could be attributed to the higher reactivity of the HIFs.

Enhanced electrochemical performance in terms of cyclability, specific capacity, and high rate were also achieved by using high index {104} faceted rhombohedral α-Fe_2O_3 as catalyst.[313] Deng *et al*. successfully prepared rhombohedral α-Fe_2O_3 by using $FeCl_3$ as the precursor in presence of 1-propanol under hydrothermal condition without any additives. During the growth process, hydrolysis of $FeCl_3$ under hydrothermal condition produced H^+ and Cl^- ions which are responsible for further etching of the rhombohedral structures. It is noted that etching process preferentially occurred on the edges of rhombohedral structure compared to smooth surface with low surface energy and ultimately produced high index {104} faceted α-Fe_2O_3. The materials exhibited high specific capacity of 550 mAh/g after 120 cycles at a rate of 200 mA/g because of the high surface energy of HIFs.

3. 2. 3. Cobalt Oxides

Li *et al*. have demonstrated the synthesis of differently shaped Co_3O_4 nanocrystals exposing different crystal planes via hydrothermal process of cobalt hydroxide precursor and subsequent direct thermal decomposition.[314] The catalytic property of {112} facet dominant Co_3O_4 nanosheet for methane combustion is superior to that of Co_3O_4 nanobelts and cubes.

This experimental result suggests that high index {112} facet is much more reactive than low index {011} and {001} facets. Fig. 30 depicts the surface atoms arrangement of fcc Co_3O_4 nanocrystals with different facets. It is observed that the area of adjacent four brown sphere is highest in case of {112} planes to that of {001} and {011} facets which suggests that {112} facet is more open. So {112} faceted Co_3O_4 nanosheet shows superior catalytic activity for methane combustion than the other two faceted Co_3O_4 nanoparticles.

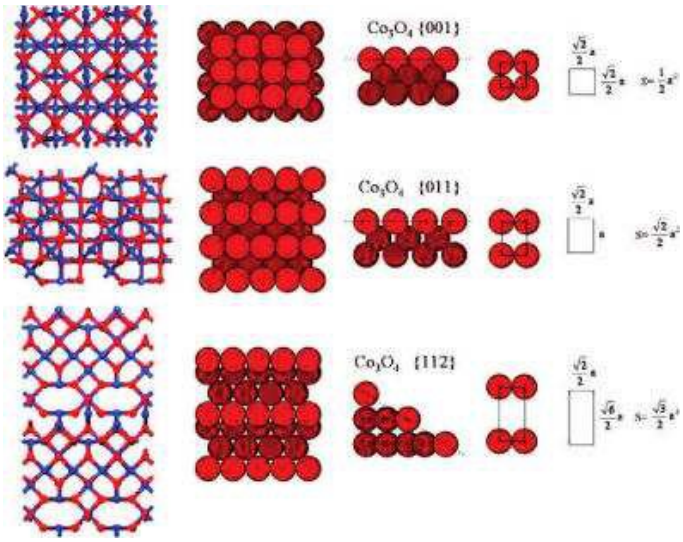

Fig. 30. Representation of surface atoms arrangement of fcc Co_3O_4 nanocrystals with different crystal facets. Reprinted with permission from ref. 314. Copyright 2008 from American Chemical Society.

3. 2. 4. Titanium Dioxides

Anatase bipyramidal TiO_2 nanocrystals bound by HIFs were prepared by a simple solvothermal method using titanium butoxide as the Ti source in a mixed solvent containing acetic acid and N,N-dimethylformamide.[315] Interestingly, this rare bipyramidal TiO_2 nanocrystals with two asymmetric pyramids have two types HIFs: short part is bound by {201} facets whereas the long part is bound by {401} facets (Fig. 31). During the anisotropic

crystal growth process, the long end of the bipyramidal TiO_2 has a tendency to self assemble on the higher energy {401} facets to minimize the free energy and ultimately form dandelion-like hierarchical structure. In addition, the {201} surfaces were exposed to the outside of the sphere as they can probably be stabilized by acetate ion present in the system. The experimental results further demonstrated that anatase bipyramidal TiO_2 nanocrystal was used as anode material for lithium-ion batteries and showed very low initial irreversible capacity loss and superior cyclic capacity retention upon extended cycling probably due to presence of HIFs.

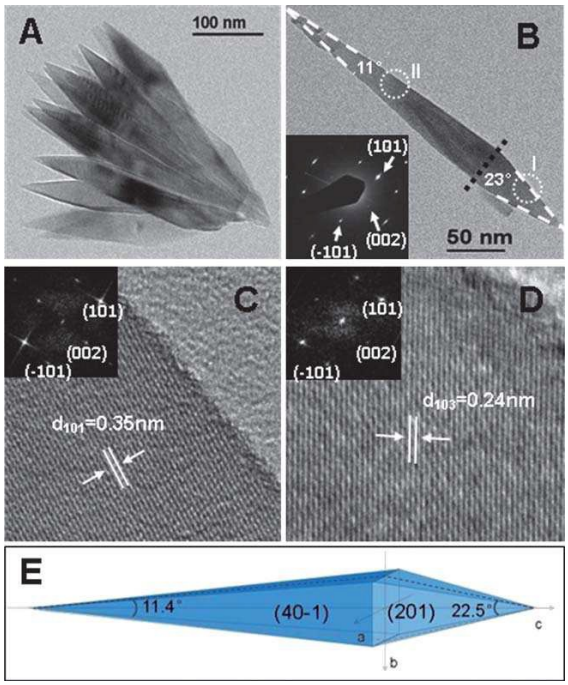

Fig. 31. (A, B) TEM images of bipyramidal TiO_2 nanocrystals (inset in B: corresponding SEAD pattern). (C and D) HRTEM images of bipyramidal TiO_2 nanocrystals taken from the dotted circles I and II in (B), respectively. (E) 3D Geometrical model of TiO_2 needles. Reprinted with permission from ref. 315. Copyright 2011 from Royal Society of Chemistry.

The use of titanium disilicide ($TiSi_2$) as a Ti source and hydrofluoric acid as crystallographic controlling agent are favourable for the synthesis of Si doped TiO_2 single crystals ($Ti_{0.89}Si_{0.11}O_2$) bound by {201} HIFs under hydrothermal condition.[316] This catalyst exhibited superior visible light induced photocatalytic activity for hydrogen evolution due to in situ incorporation of Si element to extended the light adsorption in visible region and presence of highly reactive {201} HIFs.

3. 2. 5. Tin Dioxides

The use of $SnCl_4.5H_2O$ as the precursor in an appropriate acidic environment adjusted with HCl in presence of PVP was favourable for the synthesis of octahedral SnO_2 nanoparticles with high index {221} facets under hydrothermal condition.[317] The as-synthesized octahedral SnO_2 nanoparticles served as a better catalyst for ethanol sensing due to presence of high energy {221} facets. In this study, additional HCl prevented the hydrolysis of Sn^{4+} ions to a certain extent and slow down the growth of SnO_2. In addition, PVP played a crucial role in dispersing the SnO_2 particles and prevented their aggregation with each other. From literature it is observed that the relative surface energy of {221} facets of SnO_2 (2.28 Jm^{-2}) is higher than common low-index facets such as {110} (1.401 Jm^{-2}), {101} (1.554 Jm^{-2}), and {100} (1.648 Jm^{-2}).[318] From BET surface area measurements, it is observed that {221} faceted octahedral SnO_2 has lower surface area value (11.02 m^2g^{-1}) than from elongated octahedral (18.70 m^2g^{-1}) and lance-shaped (41.49 m^2g^{-1}) SnO_2 nanoparticles. So experimental finding suggested that gas sensing property of faceted SnO_2 nanoparticles is closely related to their exposed facets but not due to their surface area.

3. 2. 6. Indium Oxides

In a roundabout way, high index {211} faceted trapezohedron-shaped (TS) In_2O_3 has been synthesized by Han *et al*. in ionic liquid.[319] This has again exhibited higher gas sensing

activity and high thermal stability due to the presence of high-density atom steps, ledges, and dangling bond.

3. 3. Polyoxometalates (POMs)

We recently reported precursor salt assisted synthesis of high index {hkl} faceted concave hexagonal plate like polyoxometalates.[320] There comes totally new information from surface etching of a well defined crystal plane for obtaining high index faceted nanocrystals. Selective etchants remove specific facets producing high index faceted crystal structures. It is found that upon addition of ammonium heptamolybdate (AHM) [etching agent] the reactivity of {001} crystal plane of hexagonal plate like ammonium copper molybdate (ACM) is much higher than {010} plane and as a result of which hexagonal plate like ACM becomes corrugated to concave hexagon with high index facet (Fig. 32). It has been shown that high index facet {422} exposed concave hexagonal ACM exhibited substantially enhanced photocatalytic activity towards congo red degradation than the other microstructures enclosed by low index facets.

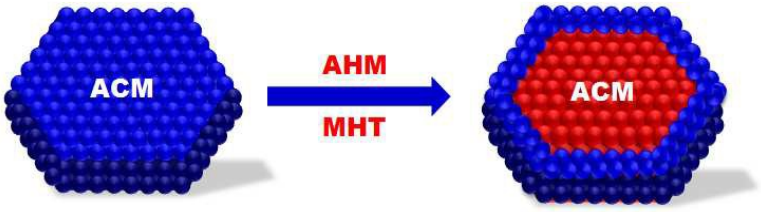

Fig. 32. Schematic illustration of preparation of high-index faceted concave hexagonal plate-like ACM from hexagonal plate-like ACM. Reprinted with permission from ref. 320. Copyright 2015 from Royal Society of Chemistry.

4. Conclusions

Herein, we have discussed the recent progress of synthetic strategy based on oxidative etching, surface capping, and kinetic/thermodynamic control for the fabrication of faceted metal, bimetallic, metal oxide, and composite nanomaterials. We have strived to explain the key factors that control the growth rate of different facets and ultimately determine the final shape of a nanocrystal. Such types of faceted nanocrystals provide a great opportunity to design new catalyst with substantially higher catalytic reactivity. Here, we have mainly emphasized on the enhanced catalytic activity of faceted oxide nanomaterials to overcome the cost effect of precious Pt-group of metals. Finally, this article explored the importance of thermodynamically unfavourable high index facets over the other low index facets in improving the catalytic reactivity of metal and metal oxides. This is mainly due to the presence of low-coordinated atoms, steps, and kinks in the high index faceted nanocrystals. Only recently a paradigm shift in photocatalysis has been explored taking hetero-junction into consideration. In future faceted hetero-junction might enlighten the world of photocatalysis to a great extent.

Acknowledgements

The authors are thankful to the UGC, DST, BRNS and CSIR New Delhi for financial assistance and IIT Kharagpur for research facilities.

References:

1. L. M. Baldyga, S. O. Blavo, C.-H. Kuo, C.-K. Tsung and J. N. Kuhn, *ACS Catal*., 2012, **2**, 2626-2629.
2. K.-L. Wu, R. Yu and X.-W. Wei, *CrystEngComm*, 2012, **14**, 7626-7632.
3. S. Panigrahi, S. Basu, S. Praharaj, S. Pande, S. Jana, A. Pal, S. K. Ghosh and T. Pal, *J. Phys. Chem. C*, 2007, **111**, 4596-4605.
4. C. Zhang, S. Y. Hwang and Z. Peng, *J. Mater. Chem. A,* 2014, **2**, 19778-19787.
5. S. Praharaj, S. Jana, S. Kundu, S. Pande and T. Pal, *J. Colloid Interface Sci*., 2009, **333**, 699-706.
6. T. K. Sau, A. Pal and T. Pal, *J. Phys. Chem. B*, 2001, **105**, 9266-9272.
7. M. Leng, C. Yu and C. Wang, *CrystEngComm*, 2012, **14**, 8454-8461.
8. H. Zhang, M. Jin, Y. Xiong, B. Lim and Y. Xia, *Acc. Chem. Res*., 2013, **46**, 1783-1794.
9. S. Jana, S. Basu, S. Pande, S. K. Ghosh and T. Pal, *J. Phys. Chem. C*, 2007, **111**, 16272-16277.
10. X. Zhang, H. Yin, J. Wang, L. Chang, Y. Gao, W. Liu and Z. Tang, *Nanoscale*, 2013, **5**, 8392-8397.
11. H. Mistry, F. Behafarid, E. Zhou, L. K. Ono, L. Zhang and C. B. Roldan, *ACS Catal*., 2014, **4**, 109-115.
12. J. Gu, Y.-W. Zhang and F. Tao, *Chem. Soc. Rev*., 2012, **41**, 8050-8065.

13. M. Pradhan, S. Sarkar, A. K. Sinha, M. Basu and T. Pal, *CrystEngComm*, 2011, **13**, 2878-2889.

14. A. K. Sinha, S. Jana, S. Pande, S. Sarkar, M. Pradhan, M. Basu, S. Saha, A. Pal and T. Pal, *CrystEngComm***,** 2009, **11**, 1210-1212.

15. S. Sarkar, A. K. Sinha, M. Pradhan, M. Basu, Y. Negishi and T. Pal, *J. Phys. Chem. C,* 2011, **115**, 1659–1673.

16. H. Rong, S. Cai, Z. Niu and Y. Li, *ACS Catal*., 2013, **37**, 1560-1563.

17. Q. Yuan, D.-B. Huang, H.-H. Wang and Z.-Y. Zhou, *Langmuir*, 2014, **30**, 5711-5715.

18. P. Wu, H. Zhang, Y. Qian, Y. Hu, H. Zhang and C. Cai, *J. Phys. Chem. C*, 2013, **117**, 19091-19100.

19. F. Can, S. Berland, S. Royer, X. Courtois and D. Duprez, *ACS Catal*., 2013, **3**, 1120-1132.

20. C. Koenigsmann, M. E. Scofield, H. Liu and S. S. Wong, *J. Phys. Chem. Lett*., 2012, **3**, 3385-3398.

21. Y. Kim, H. J. Kim, Y. S. Kim, S. M. Choi, M. H. Seo and W. B. Kim, *J. Phys. Chem. C*, 2012, **116**, 18093-18100.

22. H. Bao, Z. Zhang, Q. Hua and W. Huang, *Langmuir*, 2014, **30**, 6427-6436.

23. T. Pal, T. K. Sau and N. R. Jana, *Langmuir*, 1997, **13**, 1481-1485.

24. A. Henglein, *J. Phys. Chem.,* 1993, **97**, 5457-5471.

25. S. Kundu, S. Lau and H. Liang, *J. Phys. Chem. C,* 2009, **113**, 5150– 5156.

26. M. H. Huang, S. Rej and S.-C. Hsu, *Chem. Commun*., 2014, **50**, 1634-1644.

27. M. H. Huang and P.-H. Lin, *Adv. Funct. Mater*., 2012, **22**, 14-24.

28. K. Lee, M. Kim and H. Kim, *J. Mater. Chem*., 2010, **20**, 3791-3798.

29. Y. Xia, Y. Xiong, B. Lim and S. E. Skrabalak, *Angew. Chem., Int. Ed*., 2009, **48**, 60-113.

30. B. Lim, M. J. Jiang, J. Tao, P. H. C. Camargo, Y. Zhu and Y. Xia, *Adv. Funct. Mater*., 2009, **19**, 189-200.

31. Y. Sun and Y. Xia, *Science*, 2002, **298**, 2176–2179.

32. H. Zhang, M. Jin and Y. Xia, *Angew. Chem., Int. Ed*., 2012, **51**, 7656–7673.

33. Z. Quan, Y. Wang and J. Fang, *Acc. Chem. Res*., 2013, **46**, 191-202.

34. H. Zhang, M. Jin and Y. Xia, *Angew. Chem., Int. Ed*., 2012, **51**, 7656-7673.

35. R. A. Van Santen, *Acc. Chem. Res*., 2008, **42**, 57–66.

36. L.-M. Lyu and M. H. Huang, *J. Phys. Chem. C*, 2011, **115**, 17768-17773.

37. C. G. Read, E. M. P. Steinmiller and K.-S. Choi, *J. Am. Chem. Soc*., 2009, **131**, 12040-12041.

38. C.-H. Kuo and M. H. Huang, *Nano Today*, 2010, **5**, 106-116.

39. H. Zhu, M. L. Du, D. L. Yu, Y. Wang, M. L. Zou, C. S. Xu and Y. Q. Fu, *Dalton Trans*., 2012, **41**, 13795-13799.

40. C.-H. Kuo, Y.-C. Yang, S.-J. Gwo and M. H. Huang, *J. Am. Chem. Soc*., 2011, **133**, 1052-1057.

41. T. Luo, Q.-Q. Meng, C. Gao, X.-Y. Yu, Y. Jia, B. Sun, Z. Jin, Q.-X. Li, J.-H. Liu and X.-J. Huang, *Chem. Commun*., 2014, **50**, 15952-15955.

42. Q. Zhang and H. Wang, *ACS Catal*., 2014, **4**, 4027-4033.

43. T. Liu, P. Jiang, Q. You and S. Ye, *CrystEngComm*, 2013, **15**, 2350-2353.

44. T. P. Tyler, P. A. Lin, Y. Tian, H.-J. Gao, X. P. A. Gao, R. M. Sankaran and M. C. Hersam, *J. Phys. Chem. Lett*., 2012, **3**, 1484-1487.

45. M. R. Rahman, T. Okajima and T. Ohsaka, *Chem. Commun*., 2010, **46,** 5172-5174.

46. P. Christopher and S. Linic, *J. Am. Chem. Soc.*, 2008, **130**, 11264– 11265.

47. P. Christopher and S. Linic, *ChemCatChem*, 2010, **2**, 78–83.

48. R. Xu, D. Wang, J. Zhang and Y. Li, *Chem.–Asian J.*, 2006, **1**, 888–893.

49. R. J. Chimentˇao, I. Kirm, F. Medina, X. Rodr´ıguez, Y. Cesteros, P. Salagre and J. E. Sueiras, *Chem. Commun.*, 2004, **7**, 846–847.

50. K. Qi, Q. Wang, W. Zheng, W. Zhang and X. Cui, *Nanoscale*, 2014, **6**, 15090-15097.

51. M. Kim, Y. Kim, J. W. Hong, S. Ahn, W. Y. Kim and S. W. Han, *Chem. Commun*., 2014, **50**, 9454-9457.

52. G. Li, H. Kobayashi, S. Dekura, R. Ikeda, Y. Kubota, K. Kato, M. Takata, T. Yamamoto, S. Matsumura and H. Kitagawa, *J. Am. Chem. Soc*., 2014, **136**, 10222-10225.

53. J. Zhang, C. Feng, Y. Deng, L. Liu, Y. Wu, B. Shen, C. Zhong and W. Hu, *Chem. Mater*., 2014, **26**, 1213-1218.

54. J. Xiao, S. Liu, N. Tian, Z.-Y. Zhou, H.-X. Liu, B.-B. Xu and S.-G. Sun, *J. Am. Chem. Soc*., 2013, **135**, 18754-18757.

55. B. Zhang, D. Wang, Y. Hou, S. Yang, X. H. Yang, J. H. Zhong, J. Liu, H. F. Wang, P. Hu and H. J. Zhao, *Sci. Rep*., 2013, **3**, 1836, 7 pp..

56. L. Yang, X. Song, M. Qi, L. Xia and M. Jin, *J. Mater. Chem. A*, 2013, **1**, 7316-7320.

57. L. Ruan, H. Ramezani-Dakhel, C.-Y. Chiu, E. Zhu, Y. Li, H. Heinz and Y. Huang, *Nano Lett*., 2013, **13**, 840-846.

58. K. H. Park, K. Jang, H. J. Kim and S. U. Son, *Angew. Chem., Int. Ed.*, 2007, **46**, 1152–1155.

59. J. R. Renzas, Y. W. Zhang, W. Y. Huang and G. A. Somorjai, *Catal. Lett.*, 2009, **132**, 317–322.

60. M. J. P. Hopstaken, W. J. H. van Gennip and J. W. Niemantsverdriet, *Surf. Sci.*, 1999, **433/435**, 69–73.

61. M. J. P. Hopstaken and J. W. Niemantsverdriet, *J. Chem. Phys.*, 2000, **113**, 5457–5465.

62. M. Shao, A. Peles and J. Odell, *J. Phys. Chem. C*, 2014, **118**, 18505-18509.

63. Y. Park, Y. W. Lee, S. W. Kang and S. W. Han, *Nanoscale*, 2014, **6**, 9798-9805.

64. S.-B. Wang, W. Zhu, J. Ke, M. Lin and Y.-W. Zhang, *ACS Catal.*, 2014, **4**, 2298-2306.

65. S.-I. Choi, M. Shao, N. Lu, A. Ruditskiy, H.-C. Peng, J. Park, S. Guerrero, J. Wang, M. J. Kim and Y. Xia, *ACS Nano*, 2014, **8**, 10363-10371.

66. C.-W. Yang, K. Chanda, P.-H. Lin, Y.-N. Wang, C.-W. Liao and M. H. Huang, *J. Am. Chem. Soc.*, 2011, **133**, 19993-20000.

67. M. Jin, H. Zhang, Z. Xie and Y. Xia, *Angew. Chem., Int. Ed.*, 2011, **50**, 7850-7854.

68. Q. Zhang, J. Xu, D. Yan, S. Li, J. Lu, X. Cao and B. Wang, *Catal. Sci. Technol.*, 2013, **3**, 2016-2024.

69. Y. Zheng, J. Tao, H. Liu, J. Zeng, T. Yu, Y. Ma, C. Moran, L. Wu, Y. Zhu, J. Liu and Y. Xia, *Small*, 2011, **7**, 2307-2312.

70. R. Wang, H. He, L.-C. Liu, H.-X. Dai and Z. Zhao, *Catal. Sci. Technol.*, 2012, **2**, 575-580.

71. R. Wang, H. He, J. Wang, L. Liu and H. Dai, *Catal. Today*, 2013, **201**, 68-78.

72. Z.-N. Xu, J. Sun, C.-S. Lin, X.-M. Jiang, Q.-S. Chen, S.-Y. Peng, M.-S. Wang and G.-C. Guo, *ACS Catal.*, 2013, **3**, 118-122.

73. M. Crespo-Quesada, A. Yarulin, M. Jing, Y. Xia and L. Kiwi-Minsker, *J. Am. Chem. Soc.*, 2011, **133**, 12787-12794.

74. L. Kiwi-Minsker and M. Crespo-Quesada, *Top. Catal.*, 2012, **55**, 486-491.

75. J. Chung, C. Kim, H. Jeong, T. Yu, D. H. Binh, J. Jang, J. Lee, B. M. Kim and B. Lim, *Chem.–Asian J.*, 2013, **8**, 919-925.

76. E. Schmidt, A. Vargas, T. Mallat and A. Baiker, *J. Am. Chem. Soc.*, 2009, **131**, 12358-12367.

77. K. M. Bratlie, H. Lee, K. Komvopoulos, P. Yang and G. A. Somorjai, *Nano Lett.*, 2007, **7**, 3097–3101.

78. C.-K. Tsung, J. N. Kuhn, W. Huang, C. Aliaga, L.-I. Hung, G. A. Somorjai and P. Yang, *J. Am. Chem. Soc.*, 2009, **131**, 5816–5822.

79. Y. Tang and W. Cheng, *Langmuir*, 2013, **29**, 3125-3132.

80. C.-L. Lu, K. S. Prasad, H.-L. Wu, J.-a. A. Ho and M. H. Huang, *J. Am. Chem. Soc.*, 2010, **132**, 14546-14553.

81. J. Wang, J. Gong, Y. Xiong, J. Yang, Y. Gao, Y. Liu, X. Lu and Z. Tang, *Chem. Commun.*, 2011, **47**, 6894-6896.

82. V. Bansal, V. Li, A. P. O'Mullane and S. K. Bhargava, *CrystEngComm*, 2010, **12**, 4280-4286.

83. X. Zhang, H. Yin, J. Wang, L. Chang, Y. Gao, W. Liu and Z. Tang, *Nanoscale*, 2013, **5**, 8392-8397.

84. M. Shao, J. Odell, M. Humbert, T. Yu and Y. Xia, *J. Phys. Chem. C*, 2013, **117**, 4172-4180.

85. H. Erikson, A. Sarapuu, K. Tammeveski, J. Solla-Gullo´n and J. M. Feliu, *Electrochem. Commun.*, 2011, **13**, 734-737.

86. L. Zhang, J. Shi, M. Liu, D. Jing and L. Guo, *Chem.Commun.*, 2014, **50**, 192-194.

87. S. Yoon, M. Kim, I.-S. Kim, J.-H. Lim and B. Yoo, *J. Mater. Chem. A*, 2014, **2**, 11621-11627.

88. J. Yu, J. Fan and K. Lv, *Nanoscale*, 2010, **2**, 2144-2149.

89. Y.-e. Du, Q. Feng, C. Chen, Y. Tanaka and X. Yang, *ACS Appl. Mater. Interface*s, 2014, **6**, 16007-16019.

90. B. Liu and E. S. Aydil, *Chem. Commun*., 2011, **47**, 9507-9509.

91. H. Tang, Y. Ding, P. Jiang, H. Zhou, C. F. Guo, L. Sun, A. Yu and Z. L. Wang, *CrystEngComm*, 2011, **13**, 5052-5054.

92. F. Li, F. Gong, Y. Xiao, A. Zhang, J. Zhao, S. Fang and D. Jia, *ACS Nano*, 2013, **7**, 10482-10491.

93. T.-K. Van, H. G. Cha, C. K. Nguyen, S.-W. Kim, M.-H. Jung and Y. S. Kang, *Cryst. Growth Des*., 2012, **12**, 862-868.

94. G. Zhou, L. Li, Q. Zhang, N. Li and F. Li, *Phys. Chem. Chem. Phys*., 2013, **15**, 5582-5587.

95. G.-L. Xu, J.-T. Li, L. Huang, W. Lin and S.-G. Sun, *Nano Energy*, 2013, **2**, 394-402.

96. M. Huang, S. Weng, B. Wang, J. Hu, X. Fu and P. Liu, *J. Phys. Chem. C*, 2014, **118**, 25434-25440.

97. F. Pan, K. Wu, H. Li, G. Xu and W. Chen, *Chem. Eur. J*., 2014, **20**, 15095-15101.

98. N. Qin, Q. Xiang, H. Zhao, J. Zhang and J. Xu, *CrystEngComm*, 2014, **16**, 7062-7073.

99. J. S. Chen, D. Luan, C. M. Li, F. Y. C. Boey, S. Qiao and X. W. Lou, *Chem. Commun*., 2010, **46**, 8252-8254.

100. F. Hao, X. Wang, C. Zhou, X. Jiao, X. Li, J. Li and H. Lin, *J. Phys. Chem. C*, 2012, **116**, 19164-19172.

101. W. Peng, X. Yang, Z. Chen, J. Zhang, H. Chen, K. Zhang and L. Han, *ChemSusChem*, 2014, **7**, 172-178.

102. Y. Kwon, A. Soon, H. Han and H. Lee, *J. Mater. Chem. A*, 2015, **3**, 156-162.

103. J. Chen, B. Lim, E. P. Lee and Y. Xia, *Nano Today*, 2009, **4**, 81-95.

104. Y. Li, Q. Liu and W. Shen, *Dalton Trans*., 2011, **40**, 5811-5826.

105. G. Liu, H. G. Yang, J. Pan, Y. Q. Yang, G. Q. Lu and H.-M. Cheng, *Chem. Rev*., 2014, **114**, 9559-9612.

106. M. Cargnello, T. R. Gordon and C. B. Murray, *Chem. Rev*., 2014, **114**, 9319-9345.

107. R. Narayanan and M. A. El-Sayed, *J. Am. Chem. Soc.*, 2004, **126**, 7194–7195.

108. R. Narayanan and M. A. El-Sayed, *J. Phys. Chem. B*, 2004, **108**, 5726–5733.

109. R. Narayanan and M. A. El-Sayed, *Nano Lett.*, 2004, **4**, 1343–1348.

110. R. Narayanan and M. A. El-Sayed, *J. Phys. Chem. B*, 2005, **109**, 12663–12676.

111. M. A. Mahmoud, C. E. Tabor, M. A. El-Sayed, Y. Ding and Z. L. Wang, *J. Am. Chem. Soc.*, 2008, **130**, 4590–4591.

112. K. M. Bratlie, C. J. Kliewer and G. A. Somorjai, *J. Phys. Chem. B*, 2006, **110**, 10051–10057.

113. K. M. Bratlie, M. O. Montano, L. D. Flores, M. Paajanen and G. A. Somorjai, *J. Am. Chem. Soc.*, 2006, **128**, 12810–12816.

114. K. M. Bratlie, C. J. Kliewer and G. A. Somorjai, *J. Phys. Chem. B*, 2006, **110**, 17925–17930.

115. J. N. Kuhn, W. Y. Huang, C. K. Tsung, Y. W. Zhang and G. A. Somorjai, *J. Am. Chem. Soc.*, 2008, **130**, 14026–14027.

116. C. J. Kliewer, M. Bieri and G. A. Somorjai, *J. Phys. Chem. C*, 2008, **112**, 11373–11378.

117. N. M. Markovic, R. R. Adzic, B. D. Cahan and E. B. Yeager, *J. Electroanal. Chem*., 1994, **377**, 249.

118. B. Lim, X. Lu, M. Jiang, P. H. C. Camargo, E. C. Cho, E. P. Lee and Y. Xia, *Nano Lett*., 2008, **8**, 4043-4047.

119. C. Wang, H. Daimon, Y. Lee, J. Kim and S. Sun, *J. Am. Chem. Soc*., 2007, **129**, 6974-6975.

120. C. Wang, H. Daimon, T. Onodera, T. Koda and S. Sun, *Angew. Chem. Int. Ed*., 2008, **47**, 3588-3591.

121. C.-Y. Chiu, Y. Li, L. Ruan, X. Ye, C. B. Murray and Y. Huang, *Nat. Chem*., 2011, **3**, 393-399.

122. C.-Y. Chiu, H. Wu, Z. Yao, F. Zhou, H. Zhang, V. Ozolins and Y. Huang, *J. Am. Chem. Soc*., 2013, **135**, 15489-15500.

123. G. Berhault, L. Bisson, C. Thomazeau, C. Verdon and D. Uzio, *Appl. Catal., A*, 2007, **327**, 32–43.

124. L. Piccolo, A. Valcarcel, M. Bausach, C. Thomazeau, D. Uzio and G. Berhault, *Phys. Chem. Chem. Phys.*, 2008, **10**, 5504–5506.

125. M. M. Telkar, C. V. Rode, R. V. Chaudhari, S. S. Joshi and A. M. Nalawade, *Appl. Catal., A*, 2004, **273**, 11–19.

126. R. Ma and N. Semagina, *J. Phys. Chem. C*, 2010, **114**, 15417–15423.

127. J. Watt, S. Cheong, M. F. Toney, B. Ingham, J. Cookson, P. T. Bishop and R. D. Tilley, *ACS Nano*, 2010, **4**, 396–402.

128. D. Astruc, *Inorg. Chem.*, 2007, **46**, 1884–1894.

129. N. T. S. Phan, M. V. D. Sluys and C. W. Jones, *Adv. Synth. Catal.*, 2006, **348**, 609–679.

130. R. Narayanan and M. A. El-Sayed, *J. Am. Chem. Soc.*, 2003, **125**, 8340–8347.

131. Y. H. Chen, H. H. Hung and M. H. Huang, *J. Am. Chem. Soc.*, 2009, **131**, 9114–9121.

132. S. W. Kim, M. Kim, W. Y. Lee and T. Hyeon, *J. Am. Chem. Soc.*, 2002, **124**, 7642–7643.

133. M. Shao, T. Yu, J. Odell, M. Jin and Y. Xia, *Chem. Commun*., 2011, **47**, 6566–6568.

134. M. Jin, H. Zhang, Z. Xie and Y. Xia, *Energy Environ. Sci*., 2012, **5**, 6352-6357.

135. B. Tardy, C. Noupa, C. Leclercq, J. C. Bertolini, A. Hoareau, M. Treilleux, J. P. Faure and G. Nihoul, *J. Catal.*, 1991, **129**, 1–11.

136. G. Tourillon, A. Cassuto, Y. Jugnet, J. Massardier and J. C. Bertolini, *J. Chem. Soc., Faraday Trans.*, 1996, **92**, 4835–4841.

137. H. Conrad, G. Ertl, J. Koch and E. E. Latta, *Surf. Sci.*, 1974, **41**, 435–446.

138. J. Silvestre-Albero, G. Rupprechter and H. J. Freund, *J. Catal.*, 2006, **240**, 58–65.

139. J. Silvestre-Albero, G. Rupprechter and H. J. Freund, *J. Catal.*, 2005, **235**, 52–59.

140. J. Silvestre-Albero, G. Rupprechter and H. J. Freund, *Chem. Commun.*, 2006, **1**, 80–82.

141. M. Liu, Y. Zheng, L. Zhang, L. Guo and Y. Xia, *J. Am. Chem. Soc*., 2013, **135**, 11752-11755.

142. Y. Zhang, M. E. Grass, J. N. Kuhn, F. Tao, S. E. Habas, W. Huang, P. Yang and G. A. Somorjai, *J. Am. Chem. Soc*., 2008, **130**, 5868-5869.

143. Y. Xiong, H. Cai, B. J. Wiley, J. Wang, M. J. Kim and Y. Xia, *J. Am. Chem. Soc*., 2007, **129**, 3665-3675.

144. Y. Sun, L. Zhang, H. Zhou, Y. Zhu, E. Sutter, Y. Ji, M. H. Rafailovich and J. C. Sokolov, *Chem. Mater*., 2007, **19**, 2065-2070.

145. Q. Zhang, C. H. Moran, X. Xia, M. Rycenga, N. Li and Y. Xia, *Langmuir*, 2012, **28**, 9047-9054.

146. H.-C. Peng, S. Xie, J. Park, X. Xia and Y. Xia, *J. Am. Chem. Soc*., 2013, **135**, 3780-3783.

147. B. P. Khanal and E. R. Zubarev, *J. Am. Chem. Soc*., 2008, **130**, 12634-12635.

148. M. Pradhan and T. Pal, *Chemtracts*, 2008, **21**, 346-349.

149. C.-Y. Chiu, P.-J. Chung, K.-U. Lao, C.-W. Liao and M. H. Huang, *J. Phys. Chem. C*, 2012, **116**, 23757-23763.

150. S. Rej, K. Chanda, C.-Y. Chiu and M. H. Huang, *Chem. Eur. J*., 2014, **20**, 15991-15997.

151. M. Pradhan, S. Sarkar, A. K. Sinha, M. Basu and T. Pal, *J. Phys. Chem. C,* 2010, **114**, 16129-16142.

152. S. Xie, H. Zhang, N. Lu, M. Jin, J. Wang, M. J. Kim, Z. Xie and Y. Xia, *Nano Lett*., 2013, **13**, 6262-6268.

153. P. D. Cozzoli, T. Pellegrino and L. Manna, *Chem. Soc. Rev*., 2006, **35**, 1195−1208.

154. F. Tao, M. E. Grass, Y. Zhang, D. R. Butcher, J. R. Renzas, Z. Liu, J. Y. Chung, B. S. Mun, M. Salmeron and G. A. Somorjai, *Science*, 2008, **322**, 932−934.

155. V. R. Stamenkovic, B. S. Mun, M. Arenz, K. J. J. Mayrhofer, C. A. Lucas, G. Wang, P. N. Ross and N. M. Markovic, *Nat. Mater*., 2007, **6**, 241−247.

156. V. Mazumder, M. Chi, K. L. More and S. Sun, *Angew. Chem., Int. Ed*., 2010, **49**, 9368−9372.

157. J. Gu, Y.-W. Zhang and F. Tao, *Chem. Soc. Rev*., 2012, **41**, 8050− 8065.

158. J. Wu, P. Li, Y.-T. Pan, S. Warren, X. Yin and H. Yang, *Chem. Soc. Rev*., 2012, **41**, 8066−8074.

159. A.-X. Yin, X.-Q. Min, Y.-W. Zhang and C.-H. Yan, *J. Am. Chem. Soc*., 2011, **133**, 3816-3819.

160. X. Luo, Y. Liu, H. Zhang and B. Yang, *CrystEngComm*, 2012, **14**, 3359-3362.

161. G. Fu, L. Ding, Y. Chen, J. Lin, Y. Tang and T. Lu, *CrystEngComm*, 2014, **16**, 1606-1610.

162. J. Zeng, C. Zhu, J. Tao, M. Jin, H. Zhang, Z.-Y. Li, Y. Zhu and Y. Xia, *Angew. Chem., Int. Ed*., 2012, **51**, 2354-2358.

163. S. Xie, H.-C. Peng, N. Lu, J. Wang, M. J. Kim, Z. Xie and Y. Xia, *J. Am. Chem. Soc*., 2013, **135**, 16658-16667.

164. H. Zhang, M. Jin, Y. Xia, *Angew. Chem., Int. Ed.* 2012, **51**, 7656-7673.

165. M. Hu, J. Chen, Z. Y. Li, L. Au, G. V. Hartland, X. Li, M. Marquez and Y. Xia, *Chem. Soc. Rev*., 2006, **35**, 1084-1094.

166. M. S. Yavuz, Y. Cheng, J. Chen, C. M. Cobley, Q. Zhang, M. Rycenga, J. Xie, C. Kim, K. H. Song, A. G. Schwartz, L. V. Wang and Y. Xia, *Nat. Mater*., 2009, **8**, 935-939.

167. Z. Peng, H. You, J. Wu and H. Yang, *Nano Lett*., 2010, **10**, 1492-1496.

168. G. S. Mtraux, Y. C. Cao, R. Jin and C. A. Mirkin, *Nano Lett*., 2003, **3**, 519-522.

169. X. Lu, L. Au, J. McLellan, Z. Y. Li, M. Marquez and Y. Xia, *Nano Lett*., 2007, **7**, 1764-1769.

170. L. Au, Y. Chen, F. Zhou, P. H. C. Camargo, B. Lim, Z. Y. Li, D. S. Ginger and Y. Xia, *Nano Res*., 2008, **1**, 441-449.

171. M. McEachran, D. Keogh, B. Pietrobon, N. Cathcart, I. Gourevich, N. Coombs and V. Kitaev, *J. Am. Chem. Soc*., 2011, **133**, 8066-8069.

172. N. Fan, Y. Yang, W. Wang, L. Zhang, W. Chen, C. Zou and S. Huang, *ACS Nano*, 2012, **6**, 4072-4082.

173. S. Xie, N. Lu, Z. Xie, J. Wang, M. J. Kim, Y. Xia, *Angew. Chem., Int. Ed*., 2012, **51**, 10266-10270.

174. J. Llopis and M. Vazquez, *Electrochimi. Acta*, 1964, **9**, 1655-63.

175. D. W. Rice and J. C. Suits, *J. Appl. Phys*., 1979, **50**, 5899-901.

176. R. Jin, *Nanotechnol. Rev*., 2012, **1**, 31-56.

177. C. A. Stowell and B. A. Korgel, *Nano Lett*., 2005, **5**, 1203-1207.

178. G. S. Fonseca, A. P. Umpierre, P. F. P. Fichtner, S. R. Teixeira and J. Dupont, *Chem.-Eur. J*., 2003, **9**, 3263-3269.

179. Y. Zhang, H. Zhang, Y. Zhang, Y. Ma, H. Zhong and H. Ma, *Chem. Commun*., 2009, **43**, 6589-6591.

180. M. Rueping, R. M. Koenigs, R. Borrmann, J. Zoller, T. E. Weirich and J. Mayer, *Chem. Mater*., 2011, **23**, 2008-2010.

181. X. Xia, L. Figueroa-Cosme, J. Tao, H.-C. Peng, G. Niu, Y. Zhu and Y. Xia, *J. Am. Chem. Soc*., 2014, **136**, 10878-10881.

182. K. Chanda, S. Rej and M. H. Huang, *Chem.-Eur. J*., 2013, **19**, 16036-16043.

183. K. X. Yao, X. M. Yin, T. H. Wang and H. C. Zeng, *J. Am. Chem. Soc*., 2010, **132**, 6131-6144.

184. Y. Xu, H. Wang, Y.-F. Yu, L. Tian, W.-W. Zhao and B. Zhang, *J. Phys. Chem. C*, 2011, **115**, 15288-15296.

185. K. Chanda, S. Rej and M. H. Huang, *Nanoscale*, 2013, **5**, 12494-12501.

186. D.-F. Zhang, H. Zhang, L. Guo, K. Zheng, X.-D. Han and Z. Zhang, *J. Mater. Chem*., 2009, **19**, 5220-5225.

187. C.-H. Kuo and M. H. Huang, *J. Phys. Chem. C*, 2008, **112**, 18355-18360.

188. J.-Y. Ho and M. H. Huang, *J. Phys. Chem. C*, 2009, **113**, 14159-14164.

189. W.-C. Huang, L.-M. Lyu, Y.-C. Yang and M. H. Huang, *J. Am. Chem. Soc*., 2012, **134**, 1261-1267.

190. C.-H. Kuo, Y.-C. Yang, S. Gwo and M. H. Huang, *J. Am. Chem. Soc*., 2011, **133**, 1052-1057.

191. W.-C. Wang, L.-M. Lyu and M. H. Huang, *Chem. Mater*., 2011, **23**, 2677-2684.

192. H. Xu, W. Wang and W. Zhu, *J. Phys. Chem. B*, 2006, **110**, 13829-13834.

193. Y. Liang, L. Shang, T. Bian, C. Zhou, D. Zhang, H. Yu, H. Xu, Z. Shi, T. Zhang, L.-Z. Wu and C.-H. Tung, *CrystEngComm*, 2012, **14**, 4431-4436.

194. S. Sun, X. Song, Y. Sun, D. Deng and Z. Yang, *Catal. Sci. Technol*., 2012, **2**, 925-930.

195. Q. Hua, D. Shang, W. Zhang, K. Chen, S. Chang, Y. Ma, Z. Jiang, J. Yang and W. Huang, *Langmuir*, 2011, **27**, 665-671.

196. Q. Hua, K. Chen, S. Chang, Y. Ma and W. Huang, *J. Phys. Chem. C*, 2011, **115**, 20618-20627.

197. Y.-H. Tsai, C.-Y. Chiu and M. H. Huang, *J. Phys. Chem. C*, 2013, **117**, 24611-24617.

198. J. Ren, W. Wang, S. Sun, L. Zhang, L. Wang and J. Chang, *Ind. Eng. Chem. Res*., 2011, **50**, 10366-10369.

199. J. Pal, M. Ganguly, C. Mondal, A. Roy, Y. Negishi and T. Pal, *J. Phys. Chem. C*, 2013, **117**, 24640-24653.

200. C.-H. Kuo and M. H. Huang, *J. Am. Chem. Soc*., 2008, **130**, 12815-12820.

201. H. Zhang and J. F. Banfield, *J. Mater. Chem*., 1998, **8**, 2073-2076.

202. D. Dambournet, I. Belharouak and K. Amine, *Chem. Mater*., 2010, **22**, 1173-1179.

203. J. F. Banfield and D. R. Veblen, *Am. Mineral*., 1992, **77**, 545-57.

204. Y. Li and W. Shen, *Chem. Soc. Rev*., 2014, **43**, 1543-1574.

205. L. Liu, X. Gu, Z. Ji, W. Zou, C. Tang, F. Gao and L. Dong, *J. Phys. Chem. C*, 2013, **117**, 18578-18587.

206. X.-Q. Gong and A. Selloni, *J. Phys. Chem. B*, 2005, **109**, 19560-19562.

207. A. Vittadini, A. Selloni, F. P. Rotzinger and M. Gratzel, *Phys. Rev. Lett*., 1998, **81**, 2954-2957.

208. A. S. Barnard and L. A. Curtiss, *Nano Lett*., 2005, **5**, 1261-1266.

209. H. G. Yang and H. C. Zeng, *J. Am. Chem. Soc*., 2005, **127**, 270-278.

210. X. H. Yang, Z. Li, C. Sun, H. G. Yang and C. Li, *Chem. Mater*., 2011, **23**, 3486-3494.

211. N. Roy, Y. Sohn and D. Pradhan, *ACS Nano*, 2013, **7**, 2532-2540.

212. D. Wang, P. Kanhere, M. Li, Q. Tay, Y. Tang, Y. Huang, T. C. Sum, N. Mathews, T. Sritharan and Z. Chen, *J. Phys. Chem. C*, 2013, **117**, 22894-22902.

213. H. Xu, P. Reunchan, S. Ouyang, H. Tong, N. Umezawa, T. Kako and J. Ye, *Chem. Mater*., 2013, **25**, 405-411.

214. R. Chong, J. Li, X. Zhou, Y. Ma, J. Yang, L. Huang, H. Han, F. Zhang and C. Li, *Chem. Commun*., 2014, **50**, 165-167.

215. G. Yang, Z. Jiang, H. Shi, T. Xiao and Z. Yan, *J. Mater. Chem*., 2010, **20**, 5301–5309.

216. M. Haruta, N. Yamada, T Kobayashi and S. Iijima, *J. Catal*., 1989, **115**, 301.

217. E. Cui and G. Lu, *Int. J. Hydrogen Energy*, 2014, **39**, 7672-7685.

218. L. Liu, X. Gu, Y. Cao, X. Yao, L. Zhang, C. Tang, F. Gao and L. Dong, *ACS Catal*., 2013, **3**, 2768-2775.

219. E. Cui and G. Lu, *J. Phys. Chem. C*, 2013, **117**, 26415-26425.

220. C.-J. Jia, L.-D. Sun, F. Luo, X.-D. Han, L. J. Heyderman, Z.-G. Yan, C.-H. Yan, K. Zheng, Z. Zhang and M. Takano, *J. Am. Chem. Soc*., 2008, **130**, 16968-16977.

221. J.-E. Jorgensen, L. Mosegaard, L. E. Thomsen, T. R. Jensen and J. C. Hanson, *J. Solid State Chem*., 2007, **180**, 180-185.

222. J. Goniakowki, F. Finocchi and C. Noguera, *Rep. Progr. Phys*., 2008, **71**, 016501/1-016501/55.

223. R. C. Baetzold and H. Yang, *J. Phys. Chem. B*, 2003, **107**, 14357-14364.

224. S. Inamdar, H.-S. Choi, M.-S. Kim, K. Chaudhari, J.-S. Yu, *CrystEngComm*, 2012, **14**, 7009-7014.

225. R. Zheng, H. Gu, B. Xu, K. Fung, X. Zhang and S. Ringer, *Adv. Mater*., 2006, **18**, 2418-2421.

226. F. Lu, Q. Wu, X. Yang, L. Chen, J. Cai, C. Liang, M. Wu and P. Shen, *Phys. Chem. Chem. Phys*., 2013, **15**, 9768-9774.

227. J. Lu, Q. Peng, Z. Wang, C. Nan, L. Li and Y. Li, *J. Mater. Chem. A*, 2013, **1**, 5232-5237.

228. J. Zhu, Z. Yin, D. Yang, T. Sun, H. Yu, H. E. Hoster, H. H. Hng, H. Zhang and Q. Yan, *Energy Environ. Sci*., 2013, **6**, 987-993.

229. J. Qu, Y. Yu, C.-Y. Cao and W.-G. Song, *Chem. Eur. J.,* 2013, **19**, 11172-11177.

230. Y. Zhao, F. Pan, H. Li, T. Niu, G. Xu and W. Chen, *J. Mater. Chem. A*, 2013, **1**, 7242-7246.

231. X. Wang, J. Wang, Z. Cui, S. Wang and M. Cao, *RSC Adv*., 2014, **4**, 34387-34394.

232. W.-H. Xu, Q.-Q. Meng, C. Gao, J. Wang, Q.-X. Li, J.-H. Liu and X.-J. Huang, *Chem. Commun*., 2014, **50**, 5011-5013.

233. N. Zhao, W. Ma, Z. Cui, W. Song, C. Xu and M. Gao, *ACS Nano*, 2009, **3**, 1775-1780.

234. J. Ma, J. Teo, L. Mei, Z. Zhong, Q. Li, T. Wang, X. Duan, J. Lian and W. Zheng, *J. Mater. Chem*., 2012, **22**, 11694-11700.

235. P. Broqvist, I. Panas and H. Persson, *J. Catal*., 2002, **210**, 198-206.

236. S. C. Petitto, E. M. Marsh, G. A. Carson and M. A. Langell, *J. Mol. Catal. A*, 2008, **281**, 49-58.

237. X.-Y. Yu, Q.-Q. Meng, T. Luo, Y. Jia, B. Sun, Q.-X. Li, J.-H. Liu and X.-J. Huang, *Sci. Rep.*, 2013, **3**, 2886.

238. L. Chen, J. Hu, R. Richards, S. Prikhodko and S. Kodambaka, *Nanoscale*, 2010, **2**, 1657-1660.

239. X. Xiao, X. Liu, H. Zhao, D. Chen, F. Liu, J. Xiang, Z. Hu and Y. Li, *Adv. Mater*., 2012, **24**, 5762-5766.

240. D. Liu, X. Wang, X. Wang, W. Tian, Y. Bando and D. Golberg, *Sci. Rep*., 2013, **3**, 2543.

241. J. Wang, Z. Qiao, L. Zhang, J. Shen, R. Li, G. Yang and F. Nie, *CrystEngComm*, 2014, **16**, 8673-8677.

242. Z. Huang, G. Natu, Z. Ji, P. Hasin and Y. Wu, *J. Phys. Chem. C*, 2011, **115**, 25109-25114.

243. L. Trotochaud, J. K. Ranney, K. N. Williams and S. W. Boettcher, *J. Am. Chem. Soc*., 2012, **134**, 17253-17261.

244. G. A. Niklasson and C. G. Granqvist, *J. Mater. Chem*., 2007, **17**, 127-156.

245. G. Wang, X. Lu, T. Zhai, Y. Ling, H. Wang, Y. Tong and Y. Li, *Nanoscale*, 2012, **4**, 3123-3127.

246. J. Hu, K. Zhu, L. Chen, H. Yang, Z. Li, A. Suchopar and R. Richards, *Adv. Mater*., 2008, **20**, 267-271.

247. Z. Song, L. Chen, J. Hu and R. Richards, *Nanotechnology*, 2009, **20**, 275707/1-275707/9.

248. D. Su, M. Ford and G. Wang, *Sci. Rep*., 2012, **2**, 924, 7 pp.

249. K. Zhu, J. Hu, C. Kubel and R. Richards, *Angew. Chem., Int, Ed*., 2006, **45**, 7277-81.

250. J. Hu, K. Zhu, L. Chen, C. Kuebel and R. Richards, *J. Phys. Chem. C*., 2007, **111**, 12038-12044.

251. J. S. J. Hargreaves, G. J. Hutchings and R. W. Joyner, *Catal. Today*, 1990, **6**, 481-8.

252. J. S. J. Hargreaves, G. J. Hutchings, R. W. Joyner and C. J. Kiely, *J. Catal*., 1992, **135**, 576-95.

253. Y. N. Xu and W. Y. Ching, *Phys. Rev. B: Condens. Matter*, 1993, **48**, 4335-51.

254. J. Wrobel and J. Piechota, *Solid State Commun*., 2008, **146**, 324-329.

255. Y. Azzaz, S. Kacimi, A. Zaoui and B. Bouhafs, *Physica B: Condens. Matter*, 2008, **403**, 3154-3158.

256. G. Kresse, O. Dulub and U. Diebold, *Phys. Rev. B: Condens. Matter*, 2003, **68**, 245409/1-245409/15.

257. U. Diebold, L. V. Koplitz and O. Dulub, *Appl. Surf. Sci.*, 2004, **237**, 336-342.

258. M. Lucas, W. Mai, R. Yang, Z. L. Wang and E. Riedo, *Nano Lett.*, 2007, **7**, 1314-1317.

259. X. Wang, J. Zhou, J. Song, J. Liu, N. Xu and Z. L. Wang, *Nano Lett.*, 2006, **6**, 2768-2772.

260. N. L. Marana, V. M. Longo, E. Longo, J. B. L. Martins and J. R. Sambrano, *J. Phys. Chem. A*, 2008, **112**, 8958-8963.

261. B. Meyer and D. Marx, *Phys. Rev. B: Condens. Matter*, 2003, **67**, 035403/1-035403/11.

262. A. Wander, F. Schedin, P. Steadman, A. Norris, R. McGrath, T. S. Turner, G. Thornton and N. M. Harrison, *Phys. Rev. Lett.*, 2001, **86**, 3811-3814.

263. A. Wander and N. M. Harrison, *Surf. Sci.*, 2000, **457**, L342-L346.

264. S. Tian, F. Yang, D. Zeng and C. Xie, *J. Phys. Chem. C*, 2012, **116**, 10586-10591.

265. Q. Zhao, Q. Shen, F. Yang, H. Zhao, B. Liu, Q. Liang, A. Wei, H. Yang and S. Liu, *Sens. Actuators, B*, 2014, **195**, 71-79.

266. Y. V. Kaneti, J. Yue, X. Jiang and A. Yu, *J. Phys. Chem. C*, 2013, **117**, 13153-13162.

267. M. P. Hyman, V. M. Lebarbier, Y. Wang, A. K. Datye and J. M. Vohs, *J. Phys. Chem. C*, 2009, **113**, 7251-7259.

268. F.-R. Fan, Y. Ding, D.-Y. Liu, Z.-Q. Tian and Z. L. Wang, *J. Am. Chem. Soc*., 2009, **131**, 12036–12037.

269. E. Salje, *Acta Crystallogr*., 1977, **33**, 574−577.

270. H. Zheng, J. Z. Ou, M. S. Strano, R. B. Kaner, A. Mitchell and K. Kalantar-zadeh, *Adv. Funct. Mater*., 2011, **21**, 2175-2196.

271. F. Wang, V. C. Di and G. Pacchioni, *J. Phys. Chem. C*, 2012, **116**, 8901-8909.

272. X. Han, X. Han, L. Li and C. Wang, *New J. Chem*., 2012, **36**, 2205-2208.

273. Q.-Q. Jia, H.-M. Ji, D.-H. Wang, X. Bai, X.-H. Sun and Z.-G. Jin, *J. Mater. Chem. A*, 2014, **2**, 13602-13611.

274. Z.-G. Zhao, Z.-F. Liu and M. Miyauchi, *Chem. Commun*., 2010, **46**, 3321-3323.

275. J. Zhu, S. Wang, S. Xie and H. Li, *Chem. Commun*., 2011, **47**, 4403-4405.

276. J. Y. Zheng, G. Song, J. Hong, T. K. Van, A. U. Pawar, D. Y. Kim, C. W. Kim, Z. Haider and Y. S. Kang, *Cryst. Growth Des*., 2014, **14**, 6057-6066.

277. Y. P. Xie, G. Liu, L. Yin and H.-M. Cheng, *J. Mater. Chem*., 2012, **22**, 6746-6751.

278. G. Wang, X. Ma, B. Huang, H. Cheng, Z. Wang, J. Zhan, X. Qin, X. Zhang and Y. Dai, *J. Mater. Chem*., 2012, **22**, 21189-21194.

279. M. Meng, X. Wu, X. Zhu, L. Yang, Z. Gan, X. Zhu, L. Liu and P. K. Chu. *J. Phys. Chem. Lett*., 2014, **5**, 4298−4304.

280. J. Liu, G. Chen, Y. Yu, Y. Wu, M. Zhou, H. Zhang, C. Lv, Y. Zheng and F. He, *RSC Adv*., 2015, **5**, 44306–44312.

281. J. Pal, C. Mondal, A. K. Sasmal, M. Ganguly, Y. Negishi, T. Pal, *ACS Appl. Mater. Interfaces*, 2014, **6**, 9173-9184.

282. Y.-Q. Zhang, L.-D. Sun, W. Feng, H.-S. Wu and C.-H. Yan, *Nanoscale*, 2012, **4**, 5092-5097.

283. T. Yu, D. Y. Kim, H. Zhang and Y. Xia, *Angew. Chem., Int. Ed*., 2011, **50**, 2773-2777.

284. Z.-C. Zhang, J.-F. Hui, Z.-C. Liu, X. Zhang, J. Zhuang, X. Wang, *Langmuir*, 2012, **28**, 14845-14848.

285. J. W. Hong, S.-U. Lee, Y. W. Lee and S. W. Han, *J. Am. Chem. Soc*., 2012, **134**, 4565−4568.

286. Q. Zhang and H. Wang, *ACS Catal*., 2014, **4**, 4027−4033.

287. Q. Zhang, Y. Zhou, E. Villarreal, Y. Lin, S. Zou and H. Wang, *Nano Lett*., 2015, **15**, 4161−4169.

288. N.-F. Yu, N. Tian, Z.-Y. Zhou, L. Huang, J. Xiao, Y.-H. Wen and S.-G. Sun, *Angew. Chem. Int. Ed*., 2014, **53**, 5097 –5101.

289. X.-M. Zeng, R. Huang, Y.-H. Wen and S.-G. Sun, *Phys. Chem. Chem. Phys.,* 2015, **17**, 5751-5757.

290. Y. Lu, Y. Jiang and W. Chen, *Nanoscale*, 2014, **6**, 3309-3315.

291. A.-X. Yin, X.-Q. Min, W. Zhu, W.-C. Liu, Y.-W. Zhang and C.-H. Yan, *Chem. Eur. J*., 2012, **18**, 777-782.

292. X. Liu, W. Wang, H. Li, L. Li, G. Zhou, R. Yu, D. Wang and Y. Li, *Sci. Rep*., 2013, **3**, 1404.

293. Y. Qi, T. Bian, S.-I. Choi, Y. Jiang, C. Jin, M. Fu, H. Zhang and D. Yang, *Chem. Commun*., 2014, **50**, 560-562.

294. C. Wang, C. Lin, L. Zhang, Z. Quan, K. Sun, B. Zhao, F. Wang, N. Porter, Y. Wang and J. Fang, *Chem. Eur. J*., 2014, **20**, 1753-1759.

295. N. Moghimi, M. Abdellah, J. P. Thomas, M. Mohapatra and K. T. Leung, *J. Am. Chem. Soc*., 2013, **135**, 10958-10961.

296. M. Leng, M. Liu, Y. Zhang, Z. Wang, C. Yu, X. Yang, H. Zhang and C. Wang, *J. Am. Chem. Soc*., 2010, **132**, 17084-17087.

297. X. Wang, C. Liu, B. Zheng, Y. Jiang, L. Zhang, Z. Xie and L. Zheng, *J. Mater. Chem. A*, 2013, **1**, 282-287.

298. S. Sun, D. Deng, C. Kong, Y. Gao, S. Yang, X. Song, B. Ding and Z. Yang, *CrystEngComm*, 2011, **13**, 5993-5997.

299. S. Sun, H. Zhang, X. Song, S. Liang, C. Kong and Z. Yang, *CrystEngComm*, 2011, **13**, 6040-6044.

300. J. Yin, Z. Yu, F. Gao, J. Wang, H. Pang and Q. Lu, *Angew. Chem., Int. Ed*., 2010, **49**, 6328-6332.

301. C. J. Murphy, *Science*, 2002, **298**, 2139- 2141.

302. R. Liu, Y. Jiang, H. Fan, Q. Lu, W. Du and F. Gao, *Chem. Eur. J*., 2012, **18**, 8957-8963.

303. R. Liu, Y. Jiang, Q. Chen, Q. Lu, W. Du and F. Gao, *RSC Adv*., 2013, **3**, 8261-8268.

304. W. Wu, R. Hao, F. Liu, X. Su and Y. Hou, *J. Mater. Chem. A*, 2013, **1**, 6888-6894.

305. X. Zhou, Q. Xu, W. Lei, T. Zhang, X. Qi, G. Liu, K. Deng and J. Yu, *Small*, 2014, **10**, 674-679.

306. S. Yang, Y. Xu, Y. Sun, G. Zhang and D. Gao, *CrystEngComm*, 2012, **14**, 7915-7921.

307. J. Ouyang, J. Pei, Q. Kuang, Z. Xie and L. Zheng, *ACS Appl. Mater. Interfaces,* 2014, **6**, 12505-12514.

308. X. Liu, J. Zhang, S. Wu, D. Yang, P. Liu, H. Zhang, S. Wang, X. Yao, G. Zhu and H. Zhao, *RSC Adv*., 2012, **2**, 6178-6184.

309. Y. Yang, H. Ma, J. Zhuang and X. Wang, *Inorg. Chem*., 2011, **50**, 10143-10151.

310. Z. Liu, B. Lv, Y. Xu and D. Wu, *J. Mater. Chem. A*, 2013, **1**, 3040-3046.

311. Z. Liu, B. Lv, D. Wu, Y. Sun and Y. E. Xu, *J. Inorg. Chem*., 2012, **2012**, 4076-4081.

312. H. Liang, X. Jiang, Z. Qi, W. Chen, Z. Wu, B. Xu, Z. Wang, J. Mi and Q. Li, *Nanoscale*, 2014, **6**, 7199-7203.

313. J. Zhu, K. Y. S. Ng and D. Deng, *Cryst. Growth Des*., 2014, **14**, 2811-2817.

314. L. Hu, Q. Peng and Y. Li, *J. Am. Chem. Soc*., 2008, **130**, 16136-16137.

315. H. B. Wu, J. S. Chen, X. W. Lou and H. H. Hng, *Nanoscale*, 2011, **3**, 4082-4084.

316. L. Wu, H. B. Jiang, F. Tian, Z. Chen, C. Sun and H. G. Yang, *Chem. Commun*., 2013, **49**, 2016-2018.

317. X. Han, M. Jin, S. Xie, Q. Kuang, Z. Jiang, Y. Jiang, Z. Xie and L. Zheng, *Angew. Chem., Int. Ed*., 2009, **48**, 9180-9183.

318. B. Slater, C. R. A. Catlow, D. H. Gay, D. E. Williams and V. Dusastre, *J. Phys. Chem. B*, 1999, **103**, 10644-10650.

319. X. Han, X. Han, L. Sun, S. Gao, L. Li, Q. Kuang, Z. Xie and C. Wang, *Chem. Commun.,* 2015, **51**, 9612-9615.

320. J. Pal, M. Ganguly, C. Mondal, Y. Negishi and T. Pal, *Nanoscale*, 2015, **7**, 708-719.